SEMI-ANNUAL REPORT

(for July – December 1995)

Contract Number NAS5-31363

OCEAN OBSERVATIONS WITH EOS/MODIS:

Algorithm Development and Post Launch Studies

Howard R. Gordon

University of Miami

Department of Physics

Coral Gables, FL 33124

(Submitted January 16, 1996)

MODIS Semi-Annual Report (1 July – 31 December 1995) Contract NAS5–31363

Abstract

Several significant accomplishments were made during the present reporting period.

- An investigation of the influence of stratospheric aerosol on the performance of the atmospheric correction algorithm is nearly complete. The results indicate how the performance of the algorithm is degraded if the stratospheric aerosol is ignored. Use of the MODIS 1380 nm band to effect a correction for stratospheric aerosols was also studied. Simple algorithms such as subtracting the reflectance at 1380 nm from the visible and near infrared bands can significantly reduce the error; however, only if the diffuse transmittance of the aerosol layer is taken into account.

- The atmospheric correction code has been modified for use with absorbing aerosols. Tests of the code showed that, in contrast to nonabsorbing aerosols, the retrievals were strongly influenced by the vertical structure of the aerosol, even when the candidate aerosol set was restricted to a set appropriate to the absorbing aerosol. This will further complicate the problem of atmospheric correction in an atmosphere with strongly absorbing aerosols.

- Our whitecap radiometer system and solar aureole camera were both tested at sea and performed well.

- Investigation of a technique to remove the effects of residual instrument polarization sensitivity were initiated and applied to an instrument possessing $\sim$ 3–4 times the polarization sensitivity expected for MODIS. Preliminary results suggest that for such an instrument, elimination of the polarization effect is possible at the required level of accuracy by estimating the polarization of the top-of-atmosphere radiance to be that expected for a pure Rayleigh scattering atmosphere. This may be of significance for design of a follow-on MODIS instrument.

- W.M. Balch participated on two month-long cruises to the Arabian sea, measuring coccolithophore abundance, production, and optical properties. A thorough understanding of the relationship between calcite abundance and light scatter, in situ, will provide the basis for a generic suspended calcite algorithm.

MODIS Semi-Annual Report (1 July – 31 December 1995) Contract NAS5-31363

1. Atmospheric Correction Algorithm Development.

a. Task Objectives:

During CY 1995 there are five objectives under this task:

(i) Investigate the effects of stratospheric aerosol and/or cirrus clouds on the performance of the proposed atmospheric correction algorithm.

(ii) Complete a multilayer Monte Carlo simulation code that includes the effects of aerosol and molecular scattering polarization (a vector radiative transfer code) and sea surface roughness.

(iii) Investigate the effects of ignoring the polarization of the atmospheric light field on the performance of the proposed atmospheric correction algorithm.

(iv) Investigate the effects of vertical structure in the aerosol concentration and type on the behavior of the proposed atmospheric correction algorithm.

(v) Begin a detailed investigation of the performance of the correction algorithm in atmospheres with strongly absorbing aerosols.

b. Work Accomplished:

(i) Considerable progress was made regarding the influence of stratospheric aerosols on atmospheric correction, and the possibility of using the 1380 nm MODIS band for removing their effects. A new report covering the present status of this work is attached as Appendix 1. This supercedes that attached to the last Semi-Annual Report. Basically, it was found that including the one-way diffuse transmittance of the stratospheric aerosol made a considerable improvement in using the 1380 nm band for removal of stratospheric effects.

(ii) We have completed development and validation of a multilayer Monte Carlo code radiative transfer code that includes polarization and reported on its performance in the last Semi-Annual Report.

(iii) Using the Monte Carlo simulation code in (ii) above, we started a study of the error in the atmospheric correction algorithm caused by ignoring polarization. The results were described in the last Semi-Annual Report. As the effects of ignoring polarization appeared to be small compared to other problems, we postponed this aspect of our work in favor of concentrating on vertical structure and absorbing aerosols using the much-faster two-layer and three-layer scalar radiative transfer codes.

(iv) As described in (iii), we decided to utilize our simpler and faster two-layer and three-layer scalar radiative transfer codes to begin an examination of the effects of vertical structure. The goal was to explore the range of the effect to determine which aspect on which to focus the work to be carried out with the more complete but much slower code. This proved very fruitful.

Briefly, the reflectance of the atmosphere in the single-scattering approximation is independent of the manner in which the aerosol is distributed with altitude. However, this independence does

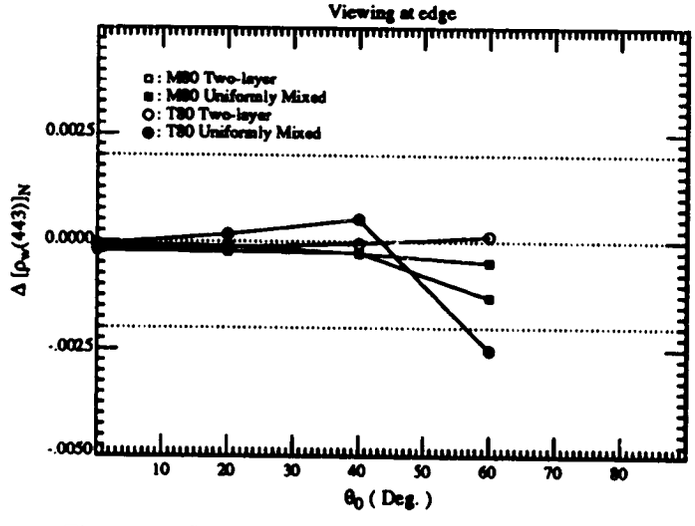

Figure 1. Effect of the vertical distribution of aerosol on $\Delta[\rho_w(443)]_N$ as a function of the solar senith angle, θ_0, at the edge of the scan for the T80 and M80 aerosol models with $\tau_a(865) = 0.2$. Note that the correction algorithm assumes that the "Two-layer" stratification is correct.

not extend to a multiple-scattering atmosphere. As the multiple-scattering atmospheric correction algorithm assumes that the aerosol is all located in the bottom layer of a two-layer atmosphere, it

is important to understand the effect of aerosol vertical structure on the correction algorithm. This has been studied by comparing the error in the algorithm when pseudo data are simulated using the "correct" two-layer model with the error when the pseudo data are simulated using a model in which the aerosol and molecular number densities have an altitude-independent mixing ratio, i.e., a uniformly mixed model. Figure 1 provides such a comparison for the M80 and T80 aerosol models with $\tau_a(865) = 0.2$. ("M80", "T80", and the "U" models used below refer to the *Shettle and Fenn* [1979] Maritime and Tropospheric models at 80% relative humidity, and their Urban models at the indicated relative humidity, respectively.) $\Delta[\rho(443)]_N$ is the error in the water-leaving reflectance at 443 nm. The goal of atmospheric correction is that the magnitude of $\Delta[\rho(443)]_N$ be less than 0.002. As these two vertical structures represent the extreme limits that might be found in nature, we conclude that the effect of an incorrect assumption regarding the vertical structure will not lead to serious errors in this case. However, as we shall see in (v), when the aerosol is strongly absorbing, the effects of vertical structure are very large.

(v) We have started a systematic study of the effects of absorbing aerosols on the performance of the atmospheric correction algorithm. Recall that that the algorithm as presently configured uses a set of 12 candidate aerosol models based on the work of *Shettle and Fenn* [1979]. These models range from nonabsorbing to weakly-absorbing aerosols. However, the presence of strongly absorbing aerosols, such as urban pollution carried by the winds over the Middle Atlantic Bight in summer, or Saharan dust transported over the Tropical North Atlantic, the algorithm does not perform well. Figure 2a compares the performance of the algorithm when the pseudo data is generated by the M80, C80, T80, and U80 aerosol models. In the figure, $\varepsilon^{(a)}(765, 865)$ is the estimated value of the aerosol reflectance ratio between 765 and 865 nm. It is fundamental to the operation of the atmospheric correction algorithm [*Gordon and Wang*, 1994]; however, it is unnecessary for the purposes of this discussion, and the reader should focus on $\Delta[\rho(443)]_N$. The first three models are

similar, but not identical to, members of the candidate aerosol set. For these, the correction is

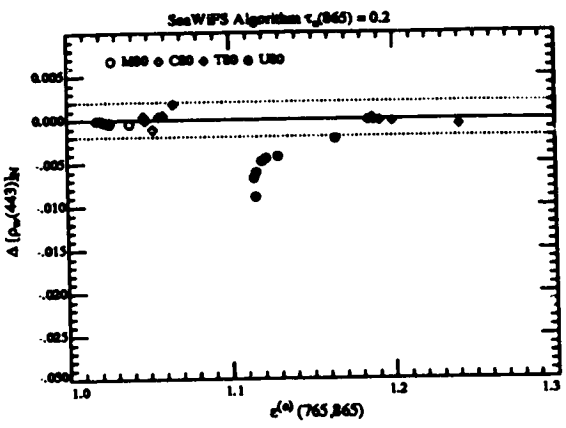

Figure 2a. $\Delta[\rho_w(443)]_N$ as a function of $\epsilon^{(a)}(765, 865)$ for $\tau_a(865) = 0.2$ and all of the viewing geometries examined in the study, using the multiple-scattering algorithm.

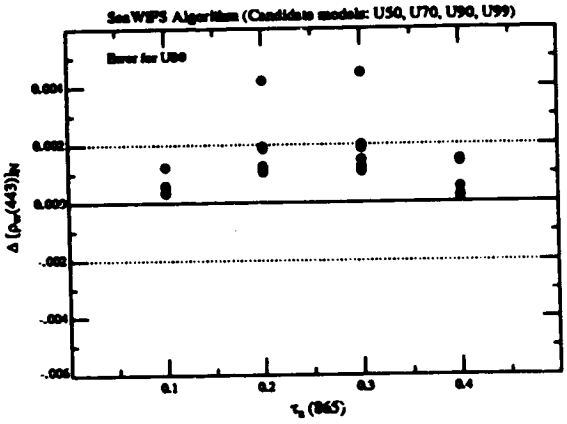

Figure 2b. $\Delta[\rho_w(443)]_N$ as a function of $\tau_a(865)$ for the U80 model, when the candidate aerosol models in the multiple-scattering algorithm are restricted to U50, U70, U90, and U99.

excellent. In contrast, the correction of the U80 model is very poor. The poor performance is due to the fact that the presence of strong absorption significantly alters the magnitude of the multiple scattering effects from that expected for the nonabsorbing or weakly-absorbing aerosols. Thus, strongly absorbing aerosols must be included in the candidate aerosol set. To test the efficacy of this, we made a set of multiple scattering lookup tables based on four candidate models U50, U70, U90, and U99. The results of the correction algorithm using these candidates are presented in Figure 2b. Note that the maximum error in Figure 2b is only twice the *minimum* error in Figure 2a. Unfortunately, if the strongly- and weakly-absorbing candidate aerosol models are mixed, the algorithm fails because it is impossible to directly determine whether or not the aerosols in an image are strongly absorbing. Thus, it appears that it is necessary to develop sets of candidate models based on a climatology of aerosol properties.

Using this restricted set of candidate models, we have also investigated the effect of vertical

structure of the aerosol. These results are presented in Figure 3. Figure 3a provides the two-layer

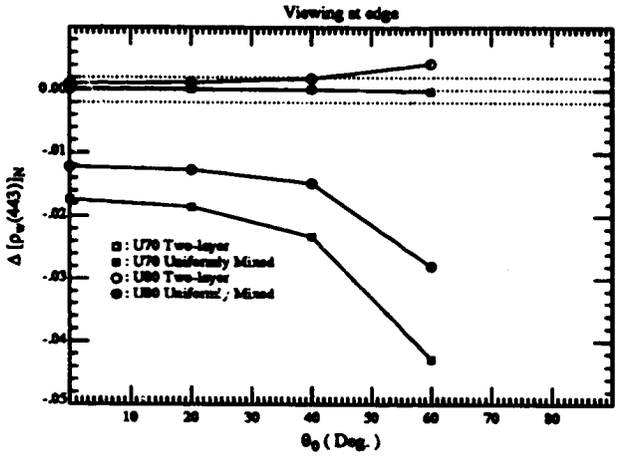

Figure 3a. Effect of the vertical distribution of aerosol on $\Delta[\rho_w(443)]_N$ as a function of θ_0 at the edge of the scan for the U80 and U70 aerosol models with $\tau_a(865) = 0.2$. The "Uniformly Mixed" case refers to a constant mixing ratio between the aerosol and molecular number densities. The "Two-layer" case places the aerosol at the sea surface as assumed by the correction algorithm.

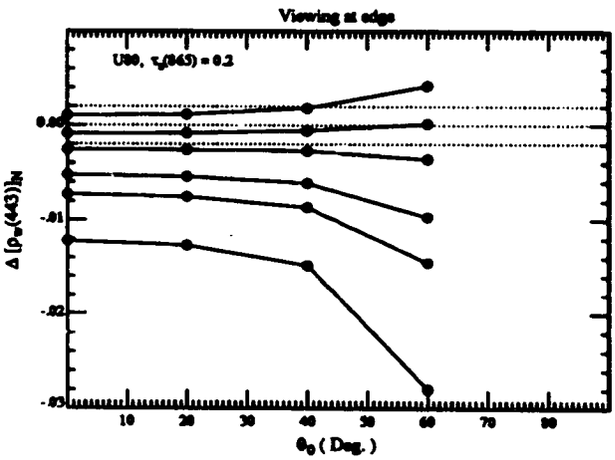

Figure 3b. Effect of the vertical distribution of aerosol on $\Delta[\rho_w(443)]_N$ as a function of θ_0 at the edge of the scan for the U80 aerosol models with $\tau_a(865) = 0.2$. Curves from top to bottom refer to situations in which the aerosol is confined to a layer just above the surface, between the surface and 1, 2, 4, and 6 km, and uniformly mixed throughout the atmosphere.

versus uniformly mixed cases for the Urban models with $\tau_a(865) = 0.2$. In this case the candidate aerosol models were restricted to U50, U70, U90, and U99, as in the results for Figure 2b. For the U80 case, the error becomes excessive, increasing by over an order of magnitude compared to the two-layer case. More disturbing is the performance of the U70 aerosol model. U70 is actually one of the candidate aerosol models in this case. When the vertical structure is the same as assumed by the algorithm, the error is negligible. In contrast, when the incorrect structure is assumed, the error becomes very large.

As we have examined only an extreme deviation from that assumed by the correction algorithm, it is of interest to quantify how the correction algorithm performs as the aerosol layer thickens from being confined just near the surface to being mixed higher in the atmosphere. Thus, the top-of-atmosphere reflectance was simulated using a two layer model with aerosol *plus* Rayleigh scattering in the lower layer and *only* Rayleigh scattering in the upper layer. The fraction of the Rayleigh scattering optical thickness assigned to the lower layer was consistent with aerosol-layer thickness of 0, 1 km, 2 km, 4 km, 6 km, and ∞. The aerosol model used in the simulations was U80, and

$\tau_a(865)$ was kept constant at 0.2. The multiple-scattering algorithm was then operated with this pseudo data using U50, U70, U90, and U99 as candidate models. The results of this exercise are provided in Figure 3b. Clearly, progressive thickening of the layer in which the aerosol resides leads to a progressive increase in the error in the retrieved water-leaving reflectance. The figure suggest that it would be necessary to know the layer thickness to within ±1 km, *as well as* to use the proper candidate model set in order to provide a correction with the desired accuracy.

This influence of vertical structure on the algorithm when the aerosol is strongly absorbing is easy to understand. The algorithm assumes all of the aerosol resides in a thin layer beneath the molecular scattering layer. As the aerosol layer thickens and encompasses more and more of the molecular scattering layer, the amount of Rayleigh scattering within the aerosol layer will increase causing an increase in the average path length of photons through the layer, and a concomitant increase in absorption. Thus, for a given τ_a, the top-of-atmosphere reflectance, ρ_t, will decrease as the thickness of the aerosol layer increases. Since the Rayleigh scattering component of the reflectance, $\rho_r \sim \lambda^{-4}$, this decrease will be relatively more in the visible than in the NIR, and the algorithm will incorrectly assess the aerosol contribution.

Finally, we have began examining the MODIS SWIR bands as a means for detecting the presence of strongly absorbing aerosols, mainly dust transported by the winds to the marine environment from desert areas, e.g., Saharan dust. At present there is no way to effect this; however, computations using Mie scattering suggest that MODIS observations of $\rho_t(\lambda)$ for $\lambda > 865$ nm, may be useful in this regard. Figure 4 compares the $\epsilon(\lambda, 865)$ for Haze C distributions (standard Junge power-law distributions, with number density $\propto$ diameter$^{-\nu}$) of nonabsorbing (liquid water) and absorbing (minerals transported over the oceans with the index of refraction taken from *d'Almeida, Koepke and Shettle* [1991]) aerosol particles. Also included on Figure 4 are computations for a log-normal distribution suggested in *d'Almeida, Koepke and Shettle* [1991] for minerals transported over large distances to the marine environment. In the figure, $\epsilon(\lambda, 865)$ is the ratio of the single-scattered aerosol reflectance at a wavelength λ to that at 865 nm. It is a key parameter in the atmospheric correction algorithm. In contrast to nonabsorbing aerosols, the mineral aerosol shows a significa[illegible]ecrease in $\epsilon(\lambda, 865)$ for $\lambda > 1.26$ μm over that extrapolated from the observed

$\epsilon(765, 865)$ and $\epsilon(1260, 865)$. This behavior of $\epsilon(\lambda, 865)$ is apparently due to the rapid decrease in the real part of the mineral refractive index beyond 1260 nm. Notwithstanding the perils of using Mie theory to predict the large-angle scattering for irregularly shaped particles [*Mishchenko and Travis*, 1994; *Mugnai and Wiscombe*, 1989] these computations suggest that it may be reasonable to try to use the short-wave infrared (SWIR) bands on MODIS to differentiate between some types of absorbing and nonabsorbing aerosols.

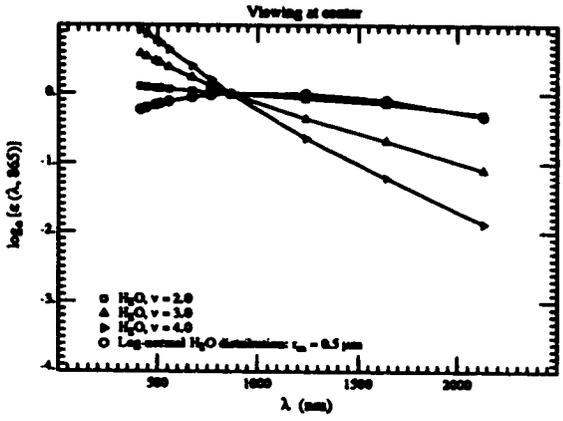

Figure 4a. $\epsilon(\lambda, 865)$ for nadir viewing with $\theta_0 = 60°$ for the Haze C models composed of liquid water.

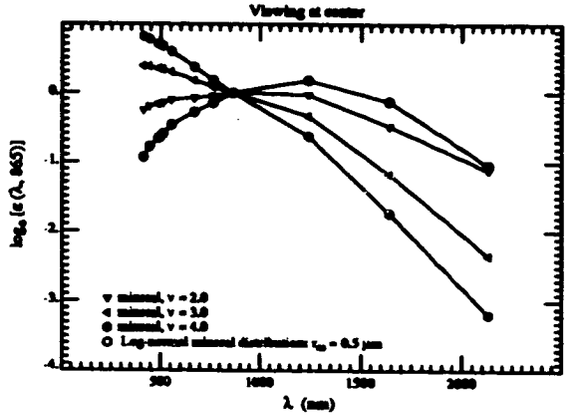

Figure 4b. $\epsilon(\lambda, 865)$ for nadir viewing with $\theta_0 = 60°$ for the Haze C models composed of absorbing minerals.

c. Data/Analysis/Interpretation: See item b above.

d. Anticipated Future Actions:

(i) We expect to finish this work in the next quarter and submit a paper to *Applied Optics*.

(ii) None. This task is now complete.

(iii) We will continue work on the effect of polarization on atmospheric correction.

(iv) We will continue work on the vertical structure problem, particularly for absorbing aerosols. Using more realistic vertical structures, we will try to estimate the accuracy with which the vertical structure is required to effect an acceptable atmospheric correction.

(v) We will continue investigating the possibility of utilizing the MODIS SWIR bands to differentiate between weakly- and strongly-absorbing aerosols. Not only is this important for the purpose of improving atmospheric correction, but also important for possibly providing a means for identifying imagery for which the quality of the atmospheric correction may be degraded, i.e., for quality assurance. However, much of the work on absorbing aerosols will be directed toward the vertical structure problem discussed under (iv).

Additional tasks for CY96. The basic correction algorithm yields the product of the diffuse transmittance t and the water-leaving reflectance ρ_w. However, t depends on the angular distribution of ρ_w. If ρ_w were uniform, t would be easy to compute, and this approximation has always been employed in the past. In a series of papers Morel and Gentili [*Morel and Gentili*, 1991; *Morel and Gentili*, 1993] studied theoretically the bidirectional effects as a function of the sun-viewing geometry and the pigment concentration. Their simulations suggest that, although the bidirectional effects nearly cancel in the estimation of the pigment concentration using radiance ratios, ρ_w can depend significantly on the solar and viewing angles. (Our major task number 3, a study of the in-water radiance distribution, experimentally addresses this problem.) We have initiated a study to understand the effect of bidirectional effects on the diffuse transmittance. This will be an area of intense work during CY 96.

e. Problems/Corrective Actions:

(i) None.

(ii) None.

(iii) None.

(iv) None.

(v) None.

f. Publications:

H.R. Gordon, Atmospheric Correction of Ocean Color Imagery in the Earth Observing System Era, Submitted to *Journal of Geophysical Research, Atmospheres.*

2. Whitecap Correction Algorithm (with K.J. Voss).

a. Task Objectives:

As described in earlier reports, a whitecap radiometer system has been built and tested to provide a database for the development and validation of the whitecap correction algorithm. The database includes spectral information as well as variables associated with the formation and occurrence of whitecaps such as wind speed, air/sea temperature, and global position.

b. Work Accomplished:

Construction, integration and calibration of the whitecap radiometer, deck cell and meteorology package has been completed. The complete system was initially tested on two one-day cruises locally in Florida waters. Although whitecaps were scarce the system simultaneously acquired the full suite of data as expected: 6 channels downwelling irradiance and upwelling radiance, air/water temperature, wind speed and direction, GPS data and UTC time. In addition, a color TV video camera mounted beside the radiometer head relayed and recorded the water, waves and whitecaps passing below. The video image was time and date stamped whenever the radiometer and the rest of the system acquired data. This provided a frame by frame reference for subsequent analysis.

In the second half of October the system was deployed on the RV McGaw for a 14-day cruise off the coast of Southern California. Weather conditions were primarily calm with diffuse overcast days — not the best for whitecap formation. However, data was taken of foam generated by the ship's wake as it moved from test station to test station. The radiometer was mounted in different positions over the side of the ship providing a data base for radiometer performance and analysis of different stages of foam development.

In early November the whitecap system was deployed on the RV Moana Wave for a 5-day cruise off the coast of the Hawaiian island of Lanai. Higher wind speeds were encountered early in

the morning and late in the evening, with some sporadic and short lived periods during the day. All in all, not many whitecaps were observed by the system to generate a good statistical database to correlate fractional coverage with wind speed or air/water temperature. This was probably due to our close proximity to the island during the cruise which most likely caused the variable and short-lived winds as well as sheltering effects.

c. Data/Analysis/Interpretation:

As stated above, spectral reflectance of foam obtained by observation of the ship's wake as it moved from test station to test station was acquired and an example of the data is shown in Figure 5. Augmented reflectance in Figure 5 is defined as the total measured reflectance minus the water

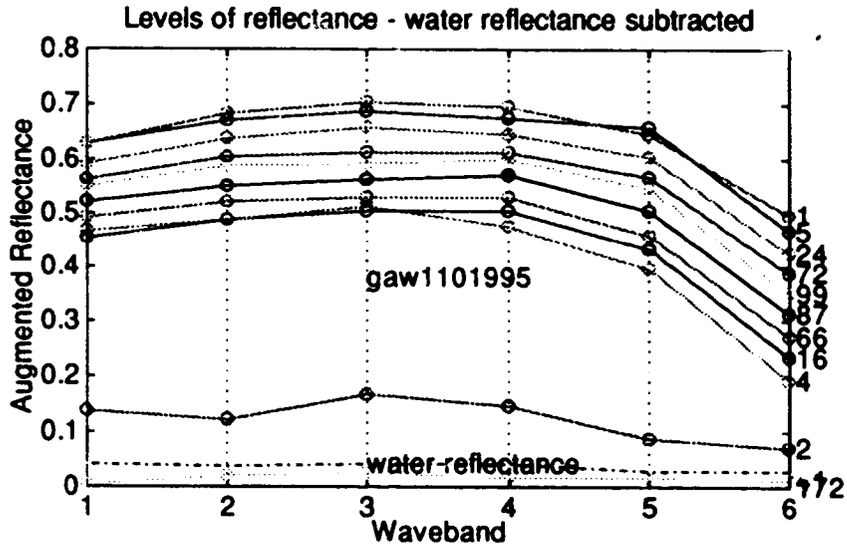

Figure 5. Spectral reflectance of a ship wake.

and sky reflectance, i.e., the reflectance of the foam and submerged bubbles. The magnitude of the augmented reflectance varies due to variations in the passing foam from submerged bubbles to thick surface foam layers. In this example, the radiometer primarily observed thick surface foam layers. The numbers on the right of the graph indicate the number of data points averaged within a certain interval of waveband 6 reflectance values. Wavebands 1 through 6 correspond to wavelengths 410,

440, 510, 550, 670 and 860 nm respectively. The water reflectance (including sky reflectance) that has been subtracted is indicated by the dash-dot line.

Interesting features to note are: (i) the consistency of the spectral shape for differing reflectance values, (ii) the drop off in bands 1 and 2, (iii) some foam reflectance values approaching 70% in bands 3 and 4. The drop off in bands in 5 and 6 are understood to be due the absorption of water at those wavelengths and should drop off more quickly when observing submerged bubbles and foam [*Schwindling*, 1995]. The drop off in bands 1 and 2 could be due to the absorption of yellow substance and has yet to be confirmed. The mean reflectance value of foam from this data set approaches 60% in bands 3 and 4, and is in agreement with those values found in the literature [*Stabeno and Monahan*, 1986]. However, reflectance values as high as 70% have been measured.

In the next example (Figure 6) data from a naturally occurring whitecap are provided. The

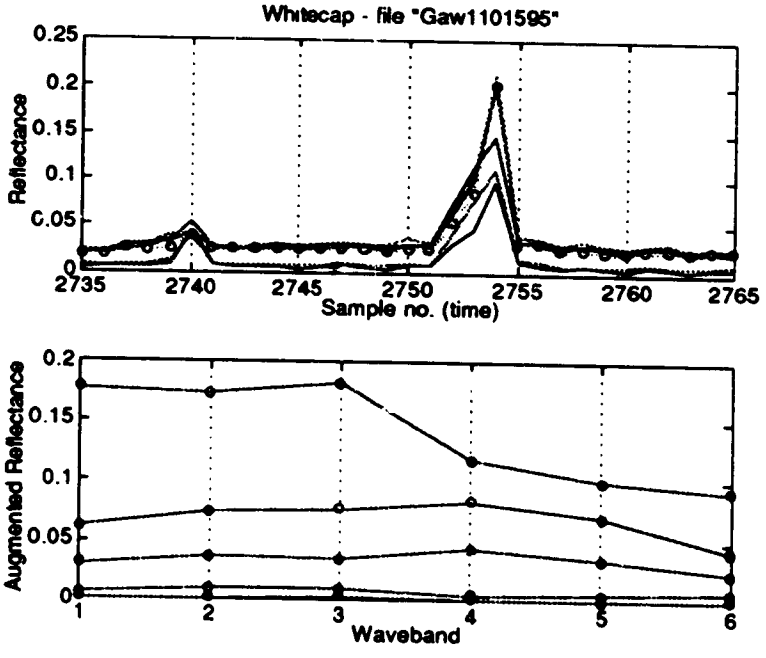

Figure 6. Spectral reflectance of a whitecap.

upper panel in Figure 6 is a continuous record of reflectance versus sample number (time). A whitecap occurs at sample points 2752 to 2754. The augmented reflectance values for the individual

wavebands are in the lower panel for sample points 2751 through 2755. The maximum reflectance value for the whitecap occurred between sample points 2753 and 2754, and was not acquired by the radiometer. The spectral shape of sample points 2752 and 2753 is consistent with the spectral shape of foam found from ship wake data. Sample point 2754 drops sharply at waveband 4. This sample point observes mainly residual (streaky) foam from the disintegrating whitecap and is most likely due to observation by that spectral channel of a slightly different area than that of the other channels.

d. Anticipated Future Actions:

In order to enhance the database to correlate fractional whitecap coverage with wind speed and air/water temperature, the video image (having a greater field of view than the radiometer) can be digitized so that the quantity of white foam pixels in every n^{th} video frame can be calculated. Calculating the ratio of white foam pixels to total pixels in every n^{th} video frame, over a sufficient number of video frame images acquired under the same wind speed, air/water temperature should provide a sufficient database to relate the whitecap coverage to wind speed, etc. This requires the procurement of a video frame grabber and software designed to analyze existing and future data, and we will be investigating this in the next period. Additional sea data will also be acquired, and we will be arranging cruises in appropriate locations.

e. Problems/Corrective Actions: None.

3. In-water Radiance Distribution (with K.J. Voss).

a. Task Objectives:

The main objective in this task is to obtain upwelling radiance distribution data at sea for a variety of solar zenith angles to understand how the water-leaving radiance varies with viewing angle and sun angle.

b. Work accomplished:

We used the RADS [*Voss*, 1989] instrument during the previously mentioned October cruise in Hawaii. The system had been augmented with polarizers to acquire the in-water polarized radiance distribution. During this cruise the system had a grounding problem and did not work, however we brought the instrument out for a short check out during another cruise in December and the instrument worked properly.

c. Data/Analysis/Interpretation: none

d. Anticipated future actions:

We will be looking for another opportunity to acquire data at sea as soon as possible. This will probably be another cruise with Dennis Clark in the Spring, or another short cruise off of Miami during this period.

e. Problems/Corrective actions: None.

f. Publications:

A. Morel, K.J. Voss, B. Gentili, Bidirectional reflectance of oceanic waters: A comparison of modeled and measured upward radiance fields, *Journal of Geophysical Research*, **100C**, 13,143–13,150 (1995).

4. Residual Instrument Polarization.

a. Task Objectives:

The basic question here is: if the MODIS responds to the state of polarization state of the incident radiance, given the polarization-sensitivity characteristics of the sensor, how much will this degrade the performance of the algorithm for atmospheric correction? Now that we have the capability of computing the polarization state of the top-of-atmosphere radiance, we shall begin to study this question. We will examine the visible sensors on MSX, which will probably be the first in-space instrument that can provide MODIS-like data. This instrument has greater polarisation sensitivity than is anticipated for MODIS, so it should provide an excellent test of our methodology.

b. Work Accomplished:

We have developed a formalism [*Gordon*, 1988] which provides the framework for removal of instrumental polarization-sensitivity effects. The difficulty with removing the polarization sensitivity error is that the polarization properties of the radiance backscattered by the aerosol are unknown. Although the details of the correction process have yet to determined, simulations of this effect for an instrument possessing $\sim$ 3–4 times the polarization sensitivity expected for MODIS are presently being carried out. Preliminary results suggest that elimination of the polarization effect is possible at the required level of accuracy by estimating the polarization of the top-of-atmosphere radiance to be that expected for a pure Rayleigh scattering atmosphere.

c. Data/Analysis/Interpretation:

See b above.

d. Anticipated Future Actions:

We will apply our techniques to MODIS.

e. Problems/Corrective Actions: None

f. Publications: None.

5. Direct Sun Glint Correction.

a. Task Objectives: None.

6. Prelaunch Atmospheric correction validation (with K.J. Voss).

a. Task Objectives:

The long-term objectives of this task are two-fold. First, we need to study the aerosol phase function and its spectral variation in order to verify the applicability of the aerosol models used in the atmospheric correction algorithm. Effecting this requires obtaining long term time series

of the aerosol optical properties in typical maritime environments. This will be achieved using a CIMEL sun/sky radiometer that can be operated in a remote environment and send data back to the laboratory via a satellite link. These are similar the radiometers used by B. Holben and Y. Kaufman. Second, we must be able to measure the aerosol optical properties from a ship during the initialization/calibration/validation cruises. The CIMEL-type instrumentation cannot be used (due to the motion of the ship) for this purpose. The required instrumentation consists of an all-sky camera (which can measure the entire sky radiance, with the exception of the solar aureole region, from a moving ship), an aureole camera (specifically designed for ship use) and a hand-held sun photometer. We have a suitable sky camera and sun photometer and had to construct an aureole camera. Our objective for this calendar year was (1) to assemble, characterize, and calibrate the solar aureole camera system, (2) to develop data acquisition software, and (3) to test the system. A second objective was to acquire a CIMEL Automatic Sun Tracking Photometer, calibrate it, and deploy it in a suitable location for studying the optical properties of aerosols over the ocean.

b. Work Accomplished:

We have constructed the solar aureole camera system, tested the system in the lab, and during October tested the instrument on a short cruise off Hawaii. The instrument worked fairly well in the Hawaii test, where several sample data sets with both the aureole camera and sky radiance distribution camera system were obtained. While preliminary data reduction has shown that the instrument performed well, there were two areas which needed improvement. Specifically, both the data acquisition triggering of the individual frames, and the filter changing, need to be improved.

The CIMEL instrument was sent to B. Holbren (NASA/GSFC) to be calibrated in comparison with his other instruments before being sent in the field. Several problems were found with the instrument, so this process took much longer than expected. At present we still hope to have a CIMEL installed in the Dry Tortugas before the end of the quarter, but if not it will be installed soon after the beginning of the new quarter.

c. Data/Analysis/Interpretation: None.

d. Anticipated Future Actions:

We will have a CIMEL instrument installed in its location in the Dry Tortugas very soon. We will also reduce the Aureole data and sky radiance data obtained during the October cruise during the next quarter.

We have initiated a critical examination of the effect of radiative transfer on "vicarious" calibration exercises. In particular, we are trying to determine the accuracy with which the radiance at the top of the atmosphere can be estimated based on measurements of sky radiance and aerosol optical thickness at the sea surface. We are carrying out a complete sensitivity analysis of the transfer process including the effects of earth curvature, polarization, sea surface roughness, and calibration error in the surface-based radiometer.

e. Problems/corrective actions: None.

f. Publications:

H.R. Gordon and T. Zhang, Columnar Aerosol Properties Over Oceans by Combining Surface and Aircraft Measurements: Simulations, *Applied Optics*, 34, 5552–5555 (1995).

H. Yang, H.R. Gordon and T. Zhang, Island perturbation to the sky radiance over the ocean: Simulations *Applied Optics* (in press)

7. Detached Coccolith Algorithm and Post Launch Studies (W.M. Balch).

a. Task Objectives:

The algorithm for retrieval of the detached coccolith concentration from the coccolithophorid, E. huxleyi is described in detail in our ATBD. The key is quantification of the backscattering coefficient of the detached coccoliths. Our earlier studies focussed on laboratory cultures to understand factors affecting the calcite-specific backscattering coefficient. To this end, the objectives of

our coccolith studies have been, under conditions of controlled growth of coccolithophores (using chemostats), to define the effect of growth rate on:

(1) the rate that coccoliths detach from cells (this is also a function of turbulence and physical shear),

(2) rates of coccolith production

(3) morphology of coccoliths

(4) volume scattering and backscatter of coccoliths

During early 1995, our work focussed on making many of the measurements to address these four objectives. Many of the data will be analyzed in 1996.

In the latter half of 1995, our work focused on shipboard measurements of suspended calcite and estimates of optical backscatter as validation of the laboratory measurements. We participated on two month-long cruises to the Arabian sea, measuring coccolithophore abundance, production, and optical properties. A thorough understanding of the relationship between calcite abundance and light scatter, in situ, will provide the basis for a generic suspended calcite algorithm. As with algorithms for chlorophyll, and primary productivity, the natural variance between growth related parameters and optical properties needs to be understood before the accuracy of the algorithm can be determined.

b. Work Accomplished:

During this last 6 months, we have performed mostly shipboard studies in the Arabian Sea. Beginning in April, we have been preparing for these cruises, shipping most of the laboratory to Muscat, Oman. In mid-July, we departed Bigelow Laboratory for Muscat, then sailed aboard the R/V Thomas Thompson for 30 days during the SW Monsoon. We sampled standing stocks, and calcification rates of coccolithophores. Samples were taken for microscopic enumeration of plated coccolithophores as well as detached coccoliths. Standing stocks of suspended calcite were also sampled on precombusted filters for later analysis using graphite furnace atomic absorption. These

samples still must be run. Finally, calcification rates were measured using a new micro-diffusion C^{14} technique. Such measurements provide perhaps the best estimate of how rapidly coccoliths are produced in the sea. This cruise returned to Muscat at the end of August.

On 20 October, we returned to Muscat for the second cruise (intermonsoon) which lasted until the end of November. We performed all of the measurements made during the first cruise, plus the weather conditions allowed us to use our new underway light scatter detection system. This device sampled the non-toxic seawater line of the ship for temperature, salinity, pH, chlorophyll fluorescence, and volume scattering (before and after the addition of a weak acid to dissolve the calcite). All data are averaged and logged every kilometer of the 3500 km trip.

The cruise also involved towing an Undulating Oceanographic Recorder (UOR) which provided the vertical resolution to our surface underway studies. The UOR is towed with about 500 m of cable, and undulates over the top 100 m, providing a complete CTD profile with associated optics (up-looking and down-looking irradiance detectors at the SEAWiFS wavelengths) every 1.5 km of the 3500 km trip.

c. Data/Analysis/Interpretation:

Given the considerable time at sea, no major data analysis has been performed yet.

d. Anticipated Future Actions: Most of the data analysis will take place in the next year. The current state of the data is as follows:

(1) Suspended calcite samples still need to be run in the graphite furnace. We are currently learning operation of the instrument.

(2) Some 600 cell and coccolith counts need to be performed.

(3) All calcification data have been processed to units of gC m^{-3} d^{-1} and integrated over the water column at each station. They still need to be processed into complete sections.

(4) Turnover of the calcite particles needs to be calculated.

(5) The underway data is now processed for temperature, salinity, pH, fluorescence and backscatter (with and without calcite) averaged over each kilometer of the trip. The data currently are in files representing each leg of the 26 leg trip. Following final calibration checks, the data will be assembled into one file.

(6) Of major interest in this data set will be the relationship between calcite-dependent backscatter (b_b') and the concentration of suspended calcite or concentration of detached coccoliths. This will be of major relevance to our MODIS algorithm efforts. Besides actually checking our algorithm, the net result will be an idea of the accuracy and precision of the algorithm, exceedingly important for subsequent interpretation.

e. Problems/Corrective Actions: None

f. Publications:

Our first paper to Limnology and Oceanography on coccolithophore bio-optics has been revised and returned to the journal. The second paper of the series is being revised now.

8. Other Developments.

A study of the effect of a bright target (such as a cloud), in the field of view of the MODIS, on the behavior of the atmospheric correction and bio-optical algorithms was carried out. Near-field scatter data provided by MCST was combined with simulations of the top-of-atmosphere clear-sky radiance over the ocean to effect the study for the protoflight instrument. The results were forwarded to Wayne Esaias for transmittal to the Team Leader.

9. Publications and submissions for CY 95.

The following publications in CY 95 received support from the present contract.

K. Ding and H.R. Gordon, Analysis of the influence of O_2 "A" band absorption on atmospheric correction of ocean color imagery, *Applied Optics*, **34**, 2068–2080 (1995).

H.R. Gordon and T. Zhang, Columnar Aerosol Properties Over Oceans by Combining Surface and Aircraft Measurements: Simulations. *Applied Optics*, **34**, 5552–5555 (1995).

M. Wang and H.R. Gordon, Estimation of aerosol columnar size distribution and optical thickness from the angular distribution of radiance exiting the atmosphere: simulations, *Applied Optics*, **34** 6989–7001 (1995).

H. Yang, H.R. Gordon and T. Zhang, Island perturbation to the sky radiance over the ocean: Simulations, *Applied Optics* (In Press).

H.R. Gordon, Remote sensing of ocean color: a methodology for dealing with broad spectral bands and significant out-of-band response, *Applied Optics* (In Press).

H.R. Gordon, Atmospheric Correction of Ocean Color Imagery in the Earth Observing System Era, *Journal of Geophysical Research, Atmospheres* (Submitted).

W.M. Balch and K.A. Kilpatrick, The 1991 Coccolithophore Bloom in the Central North Atlantic I. Optical Properties and Factors Affecting Their Distribution, *Limnology and Oceanography*, (Submitted).

W.M. Balch, K.A. Kilpatrick, P. Holligan, and D. Harbour, The 1991 Coccolithophore Bloom in the Central North Atlantic II. Relating Optics to Coccolith Concentration, Their Distribution, *Limnology and Oceanography*, (Submitted).

10. References.

d'Almeida, G. A., P. Koepke and E. P. Shettle, *Atmospheric Aerosols — Global Climatology and Radiative Characteristics*, A. Deepak Publishing, Hampton, VA, 1991.

Gordon, H. R., Ocean Color Remote Sensing Systems: Radiometric Requirements, *Society of Photo-Optical Instrumentation Engineers, Recent Advances in Sensors, Radiometry, and Data Processing for Remote Sensing*, *924*, 151–167, 1988.

Gordon, H. R. and M. Wang, Influence of Oceanic Whitecaps on Atmospheric Correction of SeaWiFS, *Applied Optics*, *33*, 7754–7763, 1994.

Mishchenko, M. I. and L. D. Travis, Light scattering by polydispersions of randomly oriented spheriods with sizes comparable to wavelengths of observation, *Applied Optics*, *33*, 7206–7225, 1994.

Morel, A. and B. Gentili, Diffuse reflectance of oceanic waters: its dependence on Sun angle as influenced by the molecular scattering contribution, *Applied Optics*, *30*, 4427–4438, 1991.

Morel, A. and B. Gentili, Diffuse reflectance of oceanic waters. II. Bidirectional aspects, *Applied Optics*, *32*, 6864–6879, 1993.

Mugnai, A. and W. J. Wiscombe, Scattering from nonspherical Chebyshev particles. 3: Variability in angular scattering patterns, *Applied Optics*, *28*, 3061–3073, 1989.

Schwindling, M., Modeles et measures pour l'observation spatiale de la couleur de l'ocean: Diffusion atmospherique par les aerosols et reflexion de surface par l'ecume, 1995, Docteur de L'Universite these, Univ. des Sci. et Tech. de Lille. 245 pp.

Shettle, E. P. and R. W. Fenn, Models for the Aerosols of the Lower Atmosphere and the Effects of Humidity Variations on Their Optical Properties, Air Force Geophysics Laboratory, Hanscomb AFB, MA 01731, AFGL–TR–79-0214, 1979.

Stabeno, P. J. and E. C. Monahan, The Influence of Whitecaps on the albedo of the Sea Surface, in *Oceanic Whitecaps*, edited by E. C. Monahan and G. M. Niocaill, pp. 261–266, Reidel, Dordrecht, 1986.

Voss, K. J., Electro-optic Camera System for Measurement of the Underwater Radiance Distribution, *Optical Engineering*, *28*, 241–247, 1989.

Appendix 1

Effects of stratospheric aerosols and thin cirrus clouds on atmospheric correction of ocean color imagery: Simulations

Howard R. Gordon, Tianming Zhang, Fan He, and Kuiyuan Ding
University of Miami
Department of Physics
Coral Gables, FL 33124

Abstract

Using simulations, we determine the influence of stratospheric aerosol and thin cirrus clouds on the performance of the proposed atmospheric correction algorithm for the MODerate resolution Imaging Spectroradiometer (MODIS) data over the oceans. Further, we investigate the possibility of using the radiance exiting the top of the atmosphere in the 1.38 μm water vapor absorption band to remove their effects prior to application of the algorithm. The computations suggest that for moderate optical thicknesses in the stratosphere, i.e., $\tau_s \lesssim 0.15$, the stratospheric aerosol/cirrus cloud contamination does not seriously degrade the MODIS except for the combination of large ($\sim 60°$) solar zenith angles and large ($\sim 45°$) viewing angles, for which multiple scattering effects can be expected to be particularly severe. The performance of a hierarchy of stratospheric aerosol/cirrus cloud removal procedures for employing the 1.38 μm water vapor absorption band to correct for stratospheric aerosol/cirrus clouds, ranging from simply subtracting the reflectance at 1.38 μm from that in the visible bands, to assuming that their optical properties are known and carrying out multiple scattering computations of their effect using the 1.38 μm reflectance-derived concentration, are studied for stratospheric aerosol optical thicknesses at 865 nm as large as 0.15 and cirrus cloud optical thicknesses at 865 nm as large as 1.0. Typically, those procedures requiring the most knowledge concerning the aerosol optical properties (and also the most complex) performed the best; however, for $\tau_s \lesssim 0.15$ their performance is usually not significantly better than applying the simplest correction procedure. For cirrus clouds at large τ_s, correction is still possible, but it is necessary to know the cirrus cloud scattering phase function and to apply the most complex procedure.

1. Introduction

The radiance exiting the ocean-atmosphere system carries information on the concentration of marine phytoplankton — the first link in the marine food chain — through the variations they produce in the color of the water.[1] The flight of the Coastal Zone Color Scanner (CZCS)[2,3] was a the proof-of-concept mission to demonstrate the feasibility of quantitatively estimating the concentration of chlorophyll a, a photosynthetic pigment contained in phytoplankton and used as a surrogate for their concentration. Based on the success of the CZCS a number of instruments for ocean color measurements will be launched in the 1990's, e.g., the sea-viewing wide field-of-view sensor (SeaWiFS)[4] and the Moderate resolution Spectroradiometer (MODIS).[5]

The contribution from beneath the sea surface to the radiance exiting the ocean-atmosphere system in the visible is very small, i.e., at most 10-20% of the total in the blue and less at longer wavelengths. The remainder of the radiance is due to scattering from the atmosphere and reflection from the sea surface. Thus, it is of the utmost importance to remove these interfering effects in order to isolate the water-leaving radiance that carries the information regarding phytoplankton. This process is termed atmospheric correction. The CZCS atmospheric correction algorithm,[6] which was based on the single scattering approximation, was not sufficiently accurate to be applied to SeaWiFS and MODIS because they have far better radiometric sensitivity. Gordon and Wang[7] developed a multiple scattering correction algorithm suitable for use with these sensors. The algorithm assumes that all of the aerosol in the atmosphere is in the marine boundary layer and uses aerosol models to deal with the multiple scattering. The requirement for aerosol models stems from the fact that the magnitude of the multiple-scattering effects is model dependent. In some situations, e.g., following volcanic eruptions or when there are thin cirrus clouds present, there can be significant quantities of aerosol in the stratosphere. Although Gordon and Castaño[8] showed that the presence of the El Chichón aerosol[9] had little effect on CZCS atmospheric correction, at the higher correction accuracy required for SeaWiFS and MODIS the Gordon and Wang[7] algorithm may be degraded by the presence of stratospheric aerosol. In the case of SeaWiFS, influence of the stratospheric aerosol on the absorption by the O_2 A-band at 762 nm introduces an additional complication. This has been discussed in detail by Ding and Gordon[10] and, as there is no direct way of assessing the presence of stratospheric aerosol with SeaWiFS, we shall not discuss that sensor further here. In contrast, MODIS, which avoids the O_2 A-band, is equipped with a spectral band at 1.38 μm that can be used to assess the contamination by stratospheric aerosol. This spectral band is centered

on a strong water vapor absorption band and photons penetrating through the stratosphere will usually be absorbed by water vapor in the free troposphere.[11] Thus, any radiance measured at 1.38 μm can, in the first approximation, be assumed to be scattered by the stratospheric aerosol alone. This provides a mechanism for estimating the stratospheric contribution. In this paper we assess the degradation in atmospheric correction of MODIS resulting from the presence of stratospheric aerosols. We assume that the radiance measured at 1.38 μm is totally due to the stratosphere and examine several possibilities for using this information in the proposed atmospheric correction algorithm[7] to correct ocean color imagery.

2. The proposed SeaWIFS-MODIS atmospheric correction algorithm

In the absence of stratospheric aerosol, the total reflectance of the ocean-atmosphere system, $\rho_t(\lambda)$, measured at a wavelength λ, can be decomposed as follows:

$$\rho_t(\lambda) = \rho_r(\lambda) + \rho_a(\lambda) + \rho_{ra}(\lambda) + t(\theta_v, \lambda)\rho_w(\lambda),$$

where $\rho_r(\lambda)$ is the radiance resulting from multiple scattering by air molecules (Rayleigh scattering) in the absence of aerosols, $\rho_a(\lambda)$ is the radiance resulting from multiple scattering by aerosols in the absence of the air, and $\rho_{ra}(\lambda)$ is the interaction term between molecular and aerosol scattering.[12] In this equation, t is the diffuse transmittance of the atmosphere along the viewing direction specified by θ_v, the angle between the normal to the sea surface and the sensor.[13] Radiance arising from specular reflection of direct sunlight from the sea surface (sun glitter) has been ignored. This means that the correction cannot be valid near the glitter pattern. The influence of whitecaps has also been ignored under the assumption that their contribution can be removed, prior to application of the correction algorithm, using an estimate of the surface wind speed.[14]

The goal of the atmospheric correction is the retrieval of ρ_w from ρ_t. This is effected by measuring ρ_t in the near infrared (NIR) near 765 and 865 nm for SeaWiFS and 750 and 865 nm for MODIS. In this spectral region, the ρ_w can be taken to be zero because of the strong absorption by the water itself. ρ_r can be computed given an estimate of the atmospheric pressure, so $\rho_a + \rho_{ra}$ can be determined directly in the NIR. From a set of candidate aerosol models, the spectral variation of $\rho_a + \rho_{ra}$ in the NIR is used to select an a pair of aerosol models for accounting for multiple scattering and for determining the spectral dependence of $\rho_a + \rho_{ra}$ for extrapolation into the visible, thus providing ρ_w there.[7] In the absence of stratospheric aerosol, simulations suggest

that this algorithm will meet the goal of retrieval of ρ_w at 443 nm with an error $\lesssim$ 0.001–0.002, i.e., an error of $\lesssim$ 5% in ρ_w in the blue in very clear ocean water.

Incorporation of multiple scattering is effected through the use of lookup tables based on a large number (~33,000) radiative transfer simulations using various aerosol models[15] thought to be representative of aerosols occurring over the oceans. In the simulations it was assumed that all of the aerosol is resident in the marine boundary layer, i.e., the simulations are carried out using an accurate (error $\lesssim$ 0.1%) two-layer radiative transfer code with aerosols occupying the lower layer and molecular (Rayleigh) scattering occupying the upper layer. This vertical structure is similar to that normally found over the oceans, i.e., most of the aerosol is in the marine boundary layer.[16]

3. Simulation of the effects of stratospheric aerosol

In situations where there is significant stratospheric aerosol present, the aerosol vertical profile described in Section 2 is very unrealistic. A more realistic profile would be a three-layer atmosphere with aerosol in both the lower and upper layers and molecular scattering in the central layer. This is the profile that we adopt for simulating ρ_t in the presence of stratospheric aerosol.

We examine three different stratospheric aerosol models. The first is the background stratospheric aerosol[17] consisting of a 75% solution of H_2SO_4 with a size distribution given by

$$\frac{dn}{dD} = 81 D \exp(-9 D),$$

where dn is the number of particles per unit volume with diameters (D) in μm between D and $D + dD$. The second is the El Chichon aerosol,[9] also a 75% solution of H_2SO_4, with a size distribution:

$$\frac{dn}{dD} = 1.79386 \times 10^8 D^{12.65} \exp(-19.65 D).$$

The third represents aged volcanic ash. It consists of an absorbing mineral distributed in size according to

$$\frac{dn}{dD} = 1365.33 D \exp(-11.3137\sqrt{D})$$

with a wavelength-independent index of refraction $m = 1.50 - 0.008i$. For the background and the El Chichon aerosol, the index of refraction is taken from Palmer and Williams.[18] The final aerosol model is that for thin cirrus clouds taken from Takano and Liou.[19] In this case we assume that the scattering properties of the thin cirrus are independent of wavelength. The scattering phase

functions for these four models are presented in Figures 1a through 1d, and the spectral variation in their extinction (or stratospheric optical thickness, τ_s) is presented in Figure 2. The first three were calculated from the size distributions and the refractive indices using Mie theory. The fourth was taken from the tabulated values of Ref. 19. Note the significant spectral variation of the shape of some of the aerosol phase functions. In particular, for the background stratospheric aerosol, the phase function at 1380 nm is very uncharacteristic of the phase function in the visible and near infrared.

As suggested above, we simulated the reflectance in the presence of stratospheric aerosol using a three-layer radiative transfer code. The lower layer contained the Shettle and Fenn[15] Maritime aerosol at 80% relative humidity. This was used as the boundary layer aerosol because, in the absence of stratospheric aerosol, the performance of the atmospheric correction algorithm is excellent (error in ρ_w found by Gordon and Wang[7] was less than about 0.0005 for this aerosol) and, thus, provides an ideal choice for examination of the interfering effects of the stratospheric aerosol. The upper layer contains the stratospheric aerosol and the middle layer exhibits only molecular scattering. A Fresnel-reflecting flat sea surface constitutes the lower boundary. There is no radiance exiting the ocean, i.e., all photons penetrating the surface are absorbed. In the case of MODIS, to simulate the reflectance at 1380 nm a one-layer model with a totally absorbing lower boundary (no Fresnel reflection) was employed. The rational for this is the assumption that all radiation penetrating through the stratosphere at this wavelength is absorbed by water vapor in the troposphere, so no radiance is reflected to the top of the atmosphere from below the stratospheric layer. Note that for the purpose of utilizing the 1380 nm MODIS band to correct for the stratospheric aerosol, this is the ideal setting, i.e., all of the reflected radiance at 1380 nm is due to the stratosphere, there is no contamination from Rayleigh scattering in the free troposphere (middle layer), aerosol scattering in the marine boundary layer (lower layer), or reflection from the sea surface.

4. Procedures for correcting for stratospheric aerosol

The stratospheric aerosol contributes to the reflectance at all wavelengths. Thus, in the presence of the stratospheric aerosol layer the total reflectance will be changed from ρ_t to $\rho_t^{(s)}$, i.e.,

$$\rho_t^{(s)}(\lambda) = T(\lambda)\rho_t(\lambda) + \delta\rho_t^{(s)}(\lambda), \tag{1}$$

where $\rho_t^{(s)}$ is the reflectance of the entire ocean-atmosphere system in the presence of stratospheric aerosol, T is a "transmittance" factor that indicates the reduction in ρ_t due to the presence of the

layer, and $\delta\rho_t^{(s)}$ is the reflectance added by the layer. As we expect the stratospheric perturbation to be small,[8] our strategy for MODIS is to try to estimate $\delta\rho_t^{(s)}$ and remove it from $\rho_t^{(s)}(\lambda)$ for an estimate of $T(\lambda)\rho_t(\lambda)$. T is then estimated and the existing atmospheric correction algorithm[7] is operated with the resulting $\rho_t(\lambda)$ as the ocean-atmosphere reflectance. In this manner the existing algorithm will be used in the setting for which it was developed: a two-layer atmosphere (the effects of the third layer having been removed) with all of the aerosol in the lower layer. Thus, the goal is to be able to remove as much of $\delta\rho_t^{(s)}(\lambda)$ from $\rho_t^{(s)}(\lambda)$ as possible. It must be recognized that the division of $\rho_t^{(s)}$ into components as in Eq. (1) is somewhat arbitrary. It is made in the manner shown because our goal is to use the reflectance of the stratosphere at 1380 nm to provide a direct estimate of $\delta\rho_t^{(s)}(\lambda)$.

Using the models outlined in Section 3, we carried out simulations of $\rho_t^{(s)}(\lambda)$ for several combinations of stratospheric and boundary-layer optical depths, τ_s and τ_b, respectively. For the Background, Aged Volcanic Ash, and El Chichón aerosols, the computations were performed using a successive-order-of-scattering radiative transfer code.[20] In the case of the cirrus cloud model, a Monte Carlo code was used because the presence of considerable angular structure in the scattering phase function (Figure 1) would have required computation of too many Fourier coefficients in the azimuthal decomposition of the radiance in the successive-order-of-scattering code to provide a reliable simulation. The computations of $\rho_t^{(s)}(\lambda)$ were carried out for λ = 443, 765, 865, and 1380 nm. The computed $\rho_t^{(s)}(\lambda)$ was used as pseudo data representative of what would be measured at the top of the atmosphere.

Using the $\rho_t^{(s)}(\lambda)$ pseudo data, we examined atmospheric correction for MODIS. We considered six possibilities for utilizing the 1380 nm band for correction for stratospheric aerosols. As described in Section 3, we assumed that the reflectance at 1380 nm was totally due to the stratospheric aerosol. The six correction schemes for removal of the stratospheric aerosol component follow.

1. The "measured" reflectances at 443, 765 and 865 nm was used in the Gordon and Wang algorithm as usual, i.e., no attention was paid to the fact that a stratospheric aerosol may be present [$\rho_t^{(s)}(\lambda)$ was assumed to be $\rho_t(\lambda)$], and the error in the atmospheric correction at 443 nm was determined.

2. The presence of stratospheric aerosol was incorporated into the algorithm by simply subtracting the reflectance at 1380 nm from those at 443, 765, and 865,

i.e., $T(\lambda)\rho_t(\lambda) = \rho_t^{(s)}(\lambda) - \rho_t^{(s)}(1380)$. The values of $\rho_t(\lambda)$ were then inserted into the correction algorithm and the error in the correction at 443 nm was determined.

3. It was assumed that the spectral variation of the optical thickness of the stratospheric aerosol is known, e.g., from measurements from the surface. The reflectance at 1380 nm (due entirely to the stratospheric aerosol) was scaled by the ratio of the stratospheric optical depth at the given λ, $\tau_s(\lambda)$, to that at (or in the case of surface measurements, near) 1380 nm, and subtracted from the measured reflectances at the other wavelengths, i.e.,

$$T(\lambda)\rho_t(\lambda) = \rho_t^{(s)}(\lambda) - \frac{\tau_s(\lambda)}{\tau_s(1380)}\rho_t^{(s)}(1380)$$

The values of $\rho_t(\lambda)$ were then inserted into the correction algorithm and the error in the correction at 443 nm determined.

4. It was assumed that accurate measurements or predictions of the other optical properties of the stratospheric aerosol, the spectral scattering phase function and single scattering albedo, along with the spectral variation of the optical depth are available for the stratospheric aerosol, e.g., from inversions of $\tau_s(\lambda)$ measurements made at the surface to obtain the size distribution from which the other optical properties are computed.[9] Only the stratospheric aerosol concentration was assumed to be unknown. It is estimated based on the measurement of $\rho_t^{(s)}(1380)$. The reflectance at 1380 nm was then scaled, by the ratio of the single-scattered stratospheric aerosol reflectances at λ to that at 1380 nm, and subtracted from the reflectances in the visible and NIR, i.e.,

$$T(\lambda)\rho_t(\lambda) = \rho_t^{(s)}(\lambda) - \frac{\omega_s(\lambda)\tau_s(\lambda)p_s(\theta_v,\phi_v;\theta_0,\phi_0;\lambda)}{\omega_s(1380)\tau_s(1380)p_s(\theta_v,\phi_v;\theta_0,\phi_0;1380)}\rho_t^{(s)}(1380),$$

where

$$p_s(\theta_v,\phi_v;\theta_0,\phi_0;\lambda) = P_s(\theta_-,\lambda) + \Big(r(\theta_v) + r(\theta_0)\Big)P_s(\theta_+,\lambda),$$

$$\cos\theta_\pm = \pm\cos\theta_0\cos\theta_v - \sin\theta_0\sin\theta_v\cos(\phi_v - \phi_0),$$

and $r(\alpha)$ is the Fresnel reflectance of the interface for an incident angle α. The parameters $\tau_s(\lambda)$, $\omega_s(\lambda)$, and $P_s(\alpha,\lambda)$ are, respectively, the stratospheric aerosol optical thickness, single scattering albedo, and scattering phase function for a

scattering angle α. The angles θ_0 and ϕ_0 are, respectively, the zenith and azimuth angles of a vector from the point on the sea surface under examination (pixel) to the sun, and likewise, θ_v and ϕ_v are the zenith and azimuth angles of a vector from the pixel to the sensor. These are measured with respect to the *upward* normal so θ_v and θ_0 are both less than 90°. At 1380 nm, $r(\alpha)$ was set to zero since the radiation at this wavelength cannot interact with the surface. The resulting values of $\rho_t(\lambda)$ were then inserted into the correction algorithm and the error at 443 nm was determined. This procedure is based on the assumption that the stratospheric aerosol enhancement of ρ_t is all due to single scattering.

5. As in (4) it was assumed that all of the optical properties of the aerosol are known except the concentration. A one-layer multiple scattering code (with a totally absorbing lower surface to represent the troposphere) was used to determine $\tau_a(1380)$ from $\rho_t^{(a)}(1380)$. This determines all of the optical properties of the stratospheric aerosol. These properties were inserted into a one-layer multiple scattering code (with a Fresnel-reflecting sea surface as the lower boundary) to compute $\delta\rho_t^{(a)\prime\setminus)}$, which was subtracted from the measured reflectances $\rho_t^{(a)}(\lambda)$ to provide $T(\lambda)\rho_t(\lambda)$. The resulting values of $\rho_t(\lambda)$ were then inserted into the correction algorithm and the error at 443 nm was determined. This procedure is similar to that in procedure 4; however, the single-scattering approximation was replaced by a full multiple-scattering computation. It is based on the assumption that there is *no radiative interaction* between the stratospheric aerosol layer and the other two layers in the visible.

6. Except for the step in which $\delta\rho_t^{(a)}(\lambda)$ is removed from $\rho_t(\lambda)$, this is identical to procedure 5. Once all of the optical properties of the stratospheric aerosol are known, they were inserted into a *two-layer* multiple scattering code (as opposed to a *one-layer* code in procedure 5 above) with a Fresnel-reflecting sea surface as the lower boundary. The top layer consisted of the stratospheric aerosol and the lower layer had only Rayleigh scattering. This incorporated the Rayleigh-stratospheric aerosol interaction explicitly (albeit approximately because of the absence of the tropospheric aerosol), leaving only the Rayleigh-tropospheric aerosol and stratospheric-tropospheric aerosol interactions not addressed. After subtracting

the result of this computation from $\rho_t^{(s)}(\lambda)$, the result was inserted into the standard correction algorithm in which allowance was made for the fact that $\rho_r(\lambda)$ has already been removed along with the stratospheric component. This approach is possible because the optical properties of the Rayleigh scattering layer as well as the stratospheric aerosol layer are completely known.

These approaches clearly require increasing amounts of knowledge concerning the optical properties of the stratospheric aerosol and increasing computational complexity. Although knowledge of the stratospheric aerosol optical properties may be good in certain instances, e.g., the El Chichon aerosol,[9] in general such will not be available.

5. Results

The procedures listed in Section 4 were all designed to utilize $\rho_t^{(s)}$ at 1380 nm to remove the stratospheric contribution to ρ_t. With the exception of the first, they all require an estimate of the transmittance factor T. Unfortunately, there is no way to use Eq. (1) to determine empirically the appropriate T in a multiple scattering regime, as the contributions $T\rho_t$ and $\delta\rho_t^{(s)}$ cannot be separated. The stratosphere influences ρ_t in two ways. First, the incident solar beam is attenuated by the stratospheric layer and in the process is also rendered somewhat diffuse. Thus, ρ_t will be changed by the change in both the angular distribution and the magnitude of the solar irradiance. Second, the resulting upward radiance at the base of the stratosphere will be further attenuated upon traversing the layer and exiting the atmosphere. T is then expected to be a two-way transmittance, i.e., it will depend on both θ and θ_0. Initially, we assumed $T = 1$, which would be appropriate in the single scattering regime.

As described earlier, we simulated $\rho_t^{(s)}$ using a three-layer model of the atmosphere. The upper layer used the four stratospheric aerosol models with stratospheric optical thickness $\tau_s = 0.05$ and 0.15 at 865 nm. A Maritime aerosol (relative humidity 80%) with marine boundary-layer optical thickness $\tau_b = 0.15$ and 0.30 was placed in the lowest layer. There was no aerosol (only Rayleigh scattering) in the middle layer. Seven geometries were simulated: near-nadir viewing ($\theta_v \approx 0$) and viewing near the scan edge ($\theta_v \approx 45°$), both for solar zenith angles of 0, 20°, 40°, and 60°. $\theta_0 = 0$ and $\theta_v \approx 0$ was not examined as it would be at the center of the sun's glitter pattern.

Examination of results the individual cases revealed the following for most of the correction procedures: (1) for a given stratospheric aerosol model, the largest values of $\Delta[t\rho_w(443)]$, the resulting error in $t\rho_w$ at 443 nm, occur at the scan edge with $\theta_0 = 60°$ where one would expect the largest effect of multiple scattering; (2) for a given θ_0, the error for viewing at the scan center is usually less than the error at the scan edge; (3) the correction errors are usually negative (too much radiance has been assigned to the atmosphere) with the Aged Volcanic Ash aerosol more negative than the others, presumably due to its moderate absorption; and (4) the general patterns of the correction error as a function of θ_0 at the scan center and edge for a given model remain the same as τ_b and τ_s are varied, but patterns for different stratospheric models are not similar. As might be expected, the most complex method of dealing with the stratospheric aerosol (procedure 6 in Section 3) usually yielded the best overall correction, however, as long as $\tau_s \leq 0.05$, most of the procedures produced acceptable results (except at the scan edge). To try to understand how the algorithm would work with larger optical thicknesses, we also simulated $\rho_t^{(s)}$ for stratospheric optical thicknesses of 0.5 and 1.0 for cirrus clouds. In this case the error became excessive with none of the procedures producing satisfactory results.

In nearly all cases with $\tau_s > 0.05$ the error at the scan edge for $\theta_0 = 60°$ was far outside the acceptable limit (± 0.002) and was negative. As it is easy to show that an overestimate of T (T too large) will likely lead to a negative error in the water-leaving reflectance, we decided to attempt to model T. In the first model we assumed that most of the radiance being scattered by the stratospheric layer is scattered through small angles (Figure 1 shows that this is certainly true for cirrus clouds). This being the case, the contribution of the downward path through the stratosphere to T is just the *irradiance* (or flux) transmittance, which is identical to the diffuse transmittance $t(\theta_0)$. We then argued that the upward radiance distribution can be approximated as diffuse (albeit poorly), hence its traverse through the stratosphere is also described by the diffuse transmittance. Thus, $T(\theta_0, \theta_v) \approx t(\theta_0)t(\theta_v)$. This assumption for T led to large positive errors in the water-leaving reflectance, and therefore, T was too small. However, the pattern of the error did suggest that a better result would be obtained with $T(\theta_0, \theta_v) \approx t(\theta_0)$. This in fact works quite well, and the results using this approximation for T are provided in Figures 3–7 for all of the simulations in the study. In these figures we present histograms of the error as a function of the stratospheric aerosol removal procedure (procedures 1–6). Along the horizontal axes "No C." refers to procedure 1, "Cons." to procedure 2, "τ_s" to procedure 3, "Sing. Algorithm" to procedure 4, "3L–R–S" to procedure 5, and "3L–(R+S)" to procedure 6. The taller bars in these figures represent the

maximum value of $|\Delta[t\rho_w(\lambda)]|$ for $\lambda = 443$ nm for the seven combinations of angles. Typically, this occurs at the scan edge with $\theta_0 = 60°$. The shorter bars in the histogram represent the average of $|\Delta[t\rho_w(\lambda)]|$ for $\lambda = 443$ nm over the remaining six combinations of angles. The horizontal dashed line is the upper limit of the acceptable error, i.e., 0.002.

These results show that, even at small values of τ_s, stratospheric aerosols can degrade the performance of the atmospheric correction algorithm, particularly in geometries where multiple scattering is expected to be large. However, in such cases a very simple correction (procedure 2) can often significantly improve the results. For large τ_s, procedure 6 provides the best results, but unfortunately it requires complete understanding of the optical properties of the aerosol and is computationally intense.

6. Discussion and concluding remarks.

In this paper we have investigated the effect and removal of the presence of stratospheric aerosol on the atmospheric correction of ocean color sensors in the simplest possible situation: (1) all of the tropospheric aerosol is in the marine boundary layer; (2) all of the radiance exiting the top of the atmosphere at 1380 nm is due to scattering from the stratospheric aerosol alone; (3) there is no water vapor above the stratospheric aerosol, and (4) there is no horizontal variability in the stratospheric aerosol optical thickness. Thus, our model is an idealization, as in reality, some radiance at 1380 nm can originate from below the stratospheric aerosol either from molecular scattering in the free troposphere or possibly even from the marine boundary layer under conditions of very low relative humidity.[21] Also, there may be water vapor above thin cirrus clouds in which case their reflectance would be underestimated at 1380 nm, and cirrus typically display considerable horizontal structure.

The goal of the study was two-fold: (1) estimation the severity of the degradation of atmospheric correction using the Gordon and Wang[14] algorithm; and (2) examination of several methods of removal of the stratospheric component using the 1380 nm spectral band prior to application of the Gordon and Wang algorithm. This latter goal is of particular interest because, if it were possible to remove the stratospheric component, little or no modification of the present atmospheric correction algorithm would be required to accommodate correction for the stratospheric aerosol. To effect the study, six procedures were examined for addressing the effect of the stratospheric

aerosol ranging from simply ignoring its presence (procedure 1) to requiring full knowledge of its spectral optical properties (procedures 4–6).

As might be expected, the stratospheric aerosol correction procedure requiring full knowledge of the spectral optical properties, except the concentration which would be determined by the reflectance at 1380 nm, and employing multiple and interactive scattering between stratospheric aerosol and tropospheric molecular scattering in the visible (procedure 6) usually yielded the best overall correction at large values of τ_a when combined with the Gordon and Wang algorithm. However, at small values of τ_a this was often not significantly better than the simplest procedure (2), and sometimes worse. The fact that procedure 1, simply ignoring the stratospheric aerosol, provides a reasonable correction for small τ_a agrees with the conclusion of Gordon and Castaño[8] that the presence of the El Chichón aerosol had little effect on CZCS atmospheric correction, taking into consideration that CZCS did not require as accurate a correction as MODIS.

With the exception of cirrus clouds, these results are based on simulations assuming τ_a at 865 to be either 0.05 or 0.15 for all of the stratospheric aerosol models. Is this a realistic range? For background conditions in the stratosphere the optical thickness at 1000 nm from the Stratospheric Aerosol and Gas Experiment (SAGE) solar occultation data is typically $\lesssim 0.01$, while following a major volcanic eruption and dispersal of the aerosol, e.g., El Chichón or Pinatubo, $\tau_a \sim 0.10$ at $\sim$ 1000 nm (L. Thomason, NASA/LaRC, personal communication). Thus, in the case of the Background aerosol model (Figure 5) τ_a at 865 nm is too high by at least a factor of 5, and one would expect the error shown in Figures 5a and 5c to be much too large and Figures 5b and 5d to be nonapplicable. Because of its low τ_a, the error due to the Background stratospheric aerosol should be negligible even without correction (procedure 1). In contrast, the values of τ_a used for the El Chichón and Aged Volcanic Ash models are in the appropriate range and the results should be representative of the performance of the algorithm in the presence of aerosols with these properties. Also, it should be noted that optical thickness (τ_b) in the marine boundary layer at 865 nm rarely exceeds 0.2 in the absence of aerosol transported from deserts and/or anthropogenic aerosol sources.[32] Therefore, of the situations presented here, the most likely are those with $\tau_b(865) = 0.15$, i.e., panels *a* and *b* in Figures 3–7. With these observations in mind, we conclude that typically the error in atmospheric correction due to volcanically-produced sulfate stratospheric aerosol should be $\lesssim 0.002$ even with the simplest correction (short bars Figure 3), except near the scan edge at large solar zenith angles (long bars Figure 3), where the multiple

scattering is expected to be greatest. For the Aged Volcanic Ash aerosol, the error is larger, and τ_a would have to be somewhat smaller for procedure 2 to provide an adequate correction (Figure 4), i.e., one would have to wait for some of the ash to be removed from the atmosphere or apply the more complex procedure 6.

In the case of cirrus clouds, procedure 2 works well as long as the optical thickness is small $\lesssim 0.15$. However, when τ_a is large $\gtrsim 0.5$ procedure 2 is only slightly better than ignoring their presence completely. In order to improve the correction at large optical thicknesses, it is necessary to employ the most complex procedure (6). Using procedure 6, it is possible to make excellent atmospheric correction even when the thin cirrus clouds have τ_a as large as 1. This is rather remarkable as the perturbation caused by the presence of the cirrus cloud is no longer small. In the absence of the cirrus cloud, for $\tau_b = 0.15$, $\rho_t(\lambda) \approx 0.18$, 0.036, and 0.028 at 443, 765, and 865 nm, respectively, while $\rho_t^{(a)}(1380) \approx 0.0078, 0.024, 0.085$, and 0.17 for $\tau_a = 0.05, 0.15, 0.5$, and 1.0, respectively. Thus, even at $\tau_a = 0.15$, the cirrus contribution alone is comparable with the value of the total reflectance at 865 nm in the absence of the cirrus cloud. Unfortunately, in order to use procedure 6, the phase function of the cirrus must be provided. Clearly, an important topic for future research is to investigate the accuracy with which the phase function must be known.

The most unsatisfying aspect of this study is the fact that the appropriate transmittance T had to be determined by trial-and-error. The somewhat awkward formulation of the problem was forced by our desire to utilize the 1380 nm band on MODIS, and by using the single-scattering approximation to guide the development of the correction. In the multiple-scattering regime there is no way of even estimating T because its effect cannot be separated from that of $\delta\rho_t^{(a)}(\lambda)$; however, based on the manner in which $\rho_t^{(a)}(1380)$ is used to estimate $\delta\rho_t^{(a)}(\lambda)$, it should be possible to make an empirical determination of T for each case examined. The approximation of T with $t(\theta_0)$ that was used here works reasonably well, and is valuable because, given an estimate of the phase function, it can be easily computed as a function of τ_a, or as a function of $\rho_t^{(a)}(1380)$. Also, it should be a weak function of the aerosol phase function. Even for procedure 2, the inclusion of T is important at the lowest values of τ_a examined in this study, therefore, a model of the aerosol is actually required to apply even the simplest procedure for removing the stratospheric aerosol.

Based on the computations presented here, we recommend that procedure 2 be used for routine (small τ_a) correction of MODIS imagery for the effects of stratospheric aerosol. We also recommend that more work be carried out to better understand the transmittance factor T, and to determine

the accuracy with which the stratospheric aerosol must be modeled. For cirrus clouds, procedure 2 is fine for low τ_s; however, when τ_s becomes large, only a correction based on procedure 6 yields acceptable results.

References

[1] H. R. Gordon and A. Y. Morel, *Remote Assessment of Ocean Color for Interpretation of Satellite Visible Imagery: A Review* (Springer-Verlag, New York, 1983), 114 pp.

[2] W. A. Hovis, D. K. Clark, F. Anderson, R. W. Austin, W. H. Wilson, E. T. Baker, D. Ball, H. R. Gordon, J. L. Mueller, S. Y. E. Sayed, B. Strum, R. C. Wrigley and C. S. Yentsch, "Nimbus 7 coastal zone color scanner: system description and initial imagery," Science **210**, 60–63 (1980).

[3] H. R. Gordon, D. K. Clark, J. L. Mueller and W. A. Hovis, "Phytoplankton pigments derived from the Nimbus–7 CZCS: initial comparisons with surface measurements," Science **210**, 63–66 (1980).

[4] S. B. Hooker, W. E. Esaias, G. C. Feldman, W. W. Gregg and C. R. McClain, *SeaWiFS Technical Report Series: Volume 1, An Overview of SeaWiFS and Ocean Color* (NASA, Greenbelt, MD, Technical Memorandum 104566, July 1992).

[5] V. V. Salomonson, W. L. Barnes, P. W. Maymon, H. E. Montgomery and H. Ostrow, "MODIS: Advanced Facility Instrument for Studies of the Earth as a System," IEEE Geosci. Rem. Sens. **27**, 145–152 (1989).

[6] H. R. Gordon and D. K. Clark, "Atmospheric effects in the remote sensing of phytoplankton pigments," Boundary-Layer Meteorology **18**, 299–313 (1980).

[7] H. R. Gordon and M. Wang, "Retrieval of water-leaving radiance and aerosol optical thickness over the oceans with SeaWiFS: A preliminary algorithm," Applied Optics **33**, 443–452 (1994).

[8] H. R. Gordon and D. J. Castaño, "The Coastal Zone Color Scanner Atmospheric Correction Algorithm: Influence of El Chichón," Applied Optics **27**, 3319–3321 (1988).

[9] M. D. King, Harshvardhan and A. Arking, "A Model of the Radiative Properties of the El Chichón Stratospheric Aerosol Layer," Journal of Climate and Applied Meteorology **23**, 1121–1137 (1984).

[10] K. Ding and H. R. Gordon, "Analysis of the influence of O_2 *A*-band absorption on atmospheric correction of ocean color imagery," Applied Optics **34**, 2068–2080 (1995).

[11] B. -C. Gao, A. F. H. Goetz and W. J. Wiscombe, "Cirrus cloud detection from airborne imaging spectrometer data using the 1.38 micron water vapor band," Geophysical Research Letters **20**, 301–304 (1993).

[12] P. Y. Deschamps, M. Herman and D. Tanre, "Modeling of the atmospheric effects and its application to the remote sensing of ocean color," Applied Optics **22**, 3751–3758 (1983).

[13] H. R. Gordon, D. K. Clark, J. W. Brown, O. B. Brown, R. H. Evans and W. W. Broenkow, "Phytoplankton pigment concentrations in the Middle Atlantic Bight: comparison between ship determinations and Coastal Zone Color Scanner estimates," Applied Optics **22**, 20–36 (1983).

[14] H. R. Gordon and M. Wang, "Influence of Oceanic Whitecaps on Atmospheric Correction of SeaWiFS," Applied Optics **33**, 7754–7763 (1994).

[15] E. P. Shettle and R. W. Fenn, *Models for the Aerosols of the Lower Atmosphere and the Effects of Humidity Variations on Their Optical Properties* (Air Force Geophysics Laboratory, Hanscomb AFB, MA 01731, AFGL–TR–79-0214, 1979).

[16] Y. Sasano and E. V. Browell, "Light scattering characteristics of various aerosol types derived from multiple wavelength lidar observations," Applied Optics **28**, 1670–1679 (1989).

[17] WCP–112, *A preliminary cloudless standard atmosphere for radiation computation* (World Meteorological Organization, WMO/TD–No. 24, Geneva, 1986).

[18] K. F. Palmer and D. Williams, "Optical constants of sulfuric acid; Application to the clouds of Venus?," Applied Oprics **14**, 208–219 (1975).

[19] Y. Takano and K. N. Liou, "Solar Radiative Transfer in Cirrus Clouds. Part I: Single-Scattering and Optical Properties of Hexagonal Ice Crystals," Jour. Atm. Sci. **46**, 224–240 (1989).

[20] H. C. van de Hulst, *Multiple Light Scattering* (Academic Press, New York, 1980), 739 pp.

[21] E. Ben-Dor, "A Precaution Regarding Cirrus Cloud Detection from Airborne Imaging Spectrometer Data Using the 1.38μm Water Vapor Band," Remote Sensing of Environment **50**, 346–350 (1994).

[22] P. J. Reddy, F. W. Kreiner, J. J. Deluisi and Y. Kim, "Aerosol Optical Depths Over the Atlantic Derived From Shipboard Sunphotometer Observations During the 1988 Global Change Expedition," Global Biogeochemical Cycles 4, 225–240 (1990).

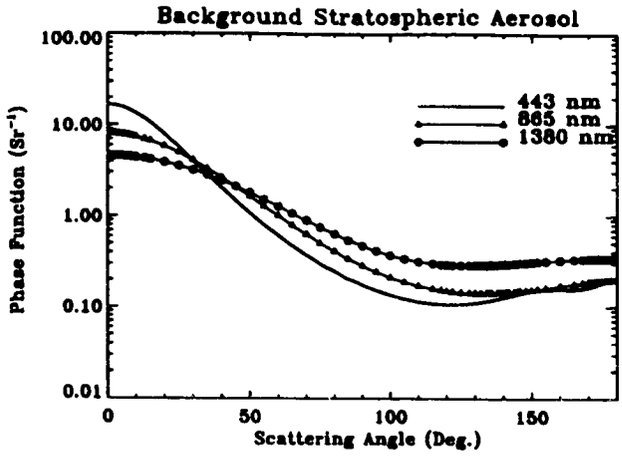

Figure 1a.

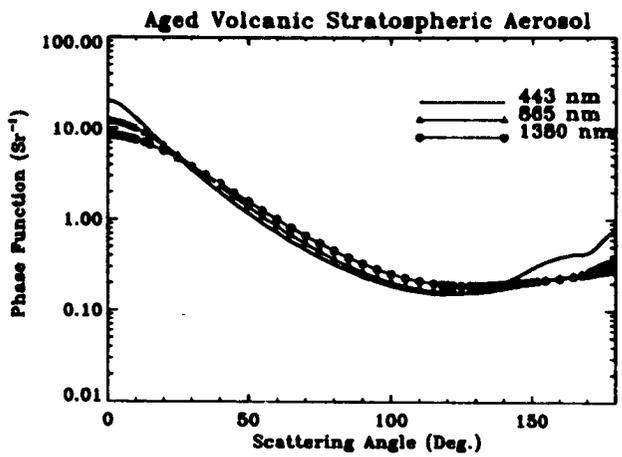

Figure 1b.

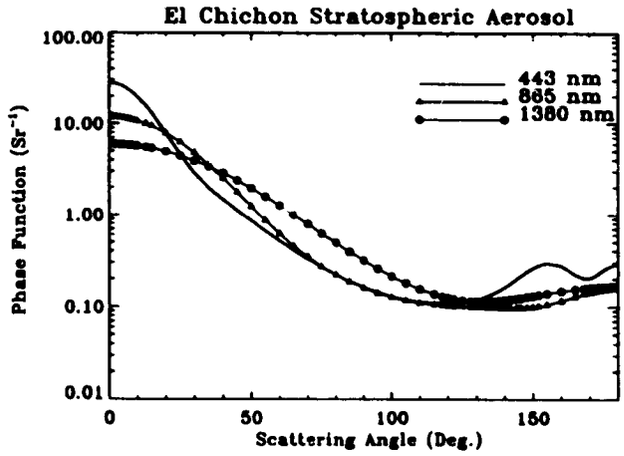

Figure 1c.

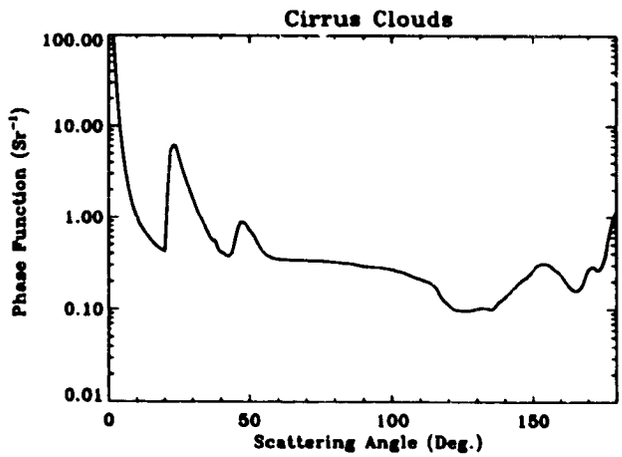

Figure 1d.

Figure 1. Phase functions for the various stratospheric aerosol models used in the study: (a) Background; (b) Aged Volcanic Ash; (c) El Chichon; and (d) thin cirrus clouds.

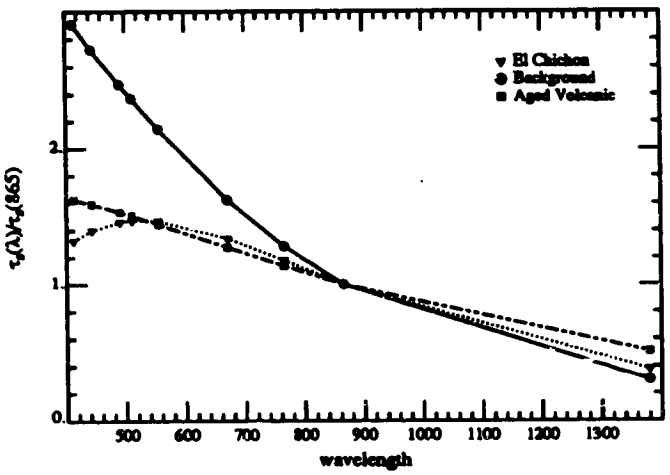

Figure 2. Spectral variation of τ_a for the various stratospheric aerosol models. The cirrus cloud model is omitted because $\tau_a(\lambda)$ is constant.

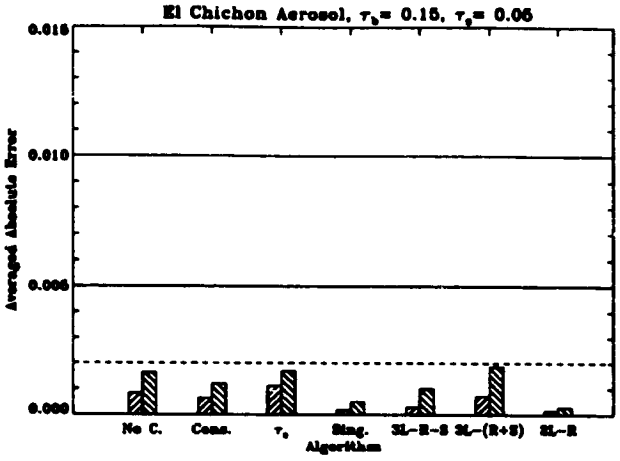

Figure 3a.

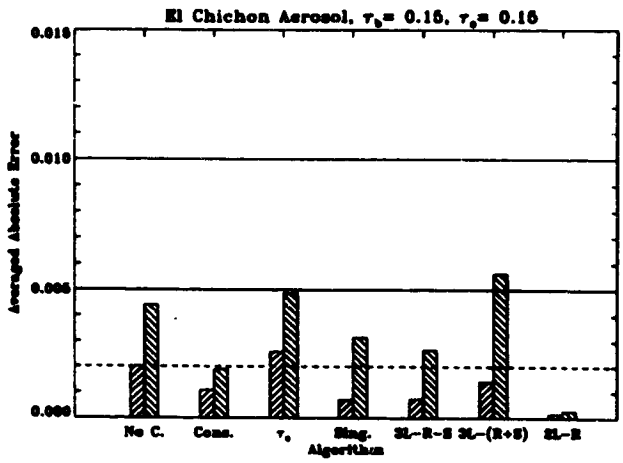

Figure 3b.

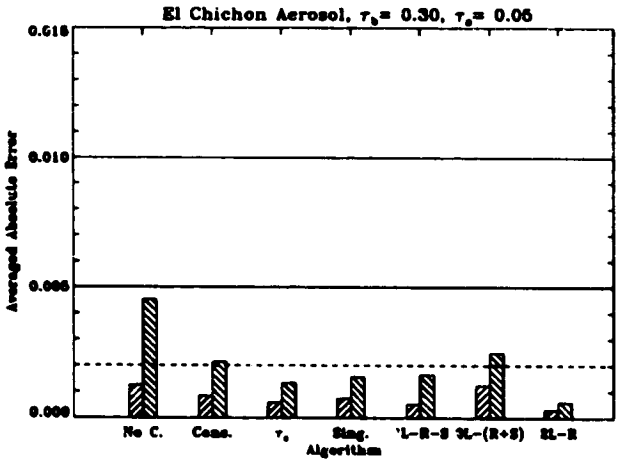

Figure 3c.

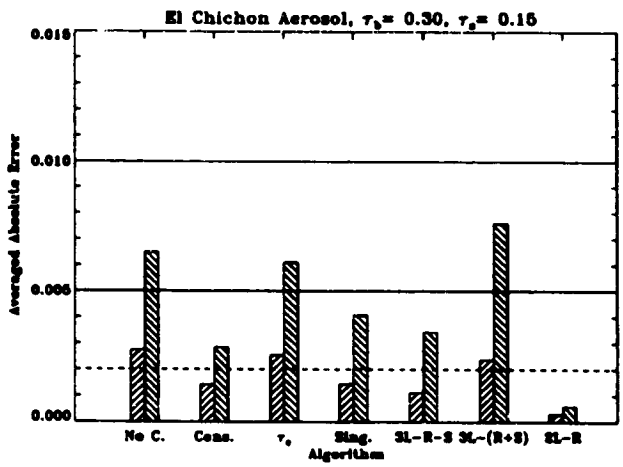

Figure 3d.

Figure 3. Histogram of the average $|\Delta t \rho_w(443)|$ (short bars) and the maximum $|\Delta t \rho_w(443)|$ (tall bars) for the El Chichon stratospheric aerosol for various combinations of τ_b and τ_s: (a) $\tau_b(865) = 0.15$, $\tau_s(865) = 0.05$; (b) $\tau_b(865) = 0.15$, $\tau_s(865) = 0.15$; (c) $\tau_b(865) = 0.30$, $\tau_s(865) = 0.05$; and (d) $\tau_b(865) = 0.30$, $\tau_s(865) = 0.15$.

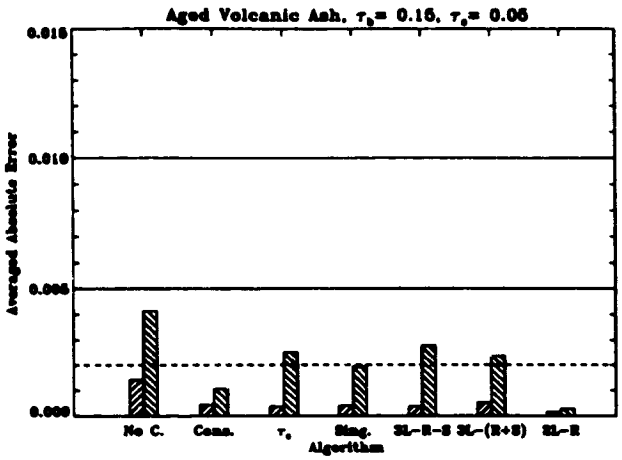

Figure 4a.

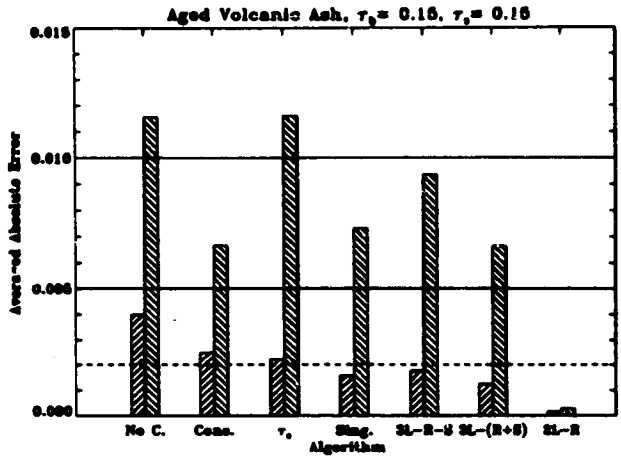

Figure 4b.

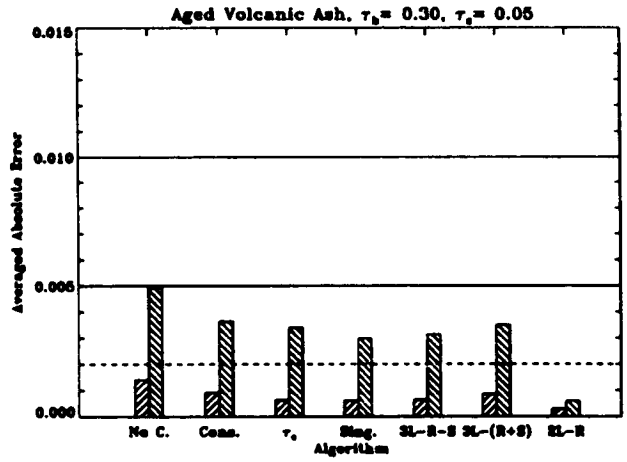

Figure 4c.

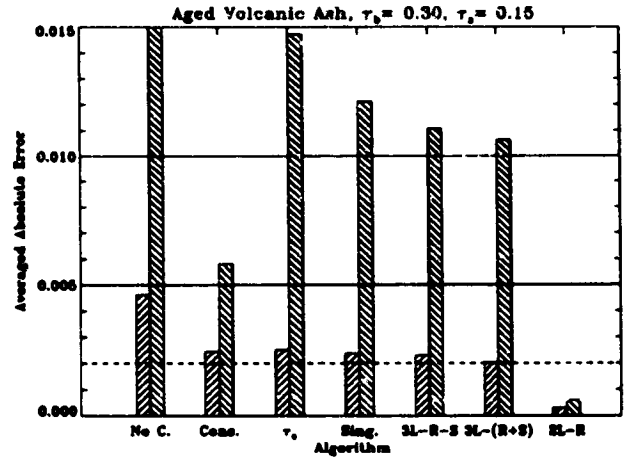

Figure 4d.

Figure 4. Histogram of the average $|\Delta t \rho_w(443)|$ (short bars) and the maximum $|\Delta t \rho_w(443)|$ (tall bars) for the Aged Volcanic Ash aerosol for various combinations of τ_b and τ_s: (a) $\tau_b(865) = 0.15$, $\tau_s(865) = 0.05$; (b) $\tau_b(865) = 0.15$, $\tau_s(865) = 0.15$; (c) $\tau_b(865) = 0.30$, $\tau_s(865) = 0.05$; and (d) $\tau_b(865) = 0.30$, $\tau_s(865) = 0.15$.

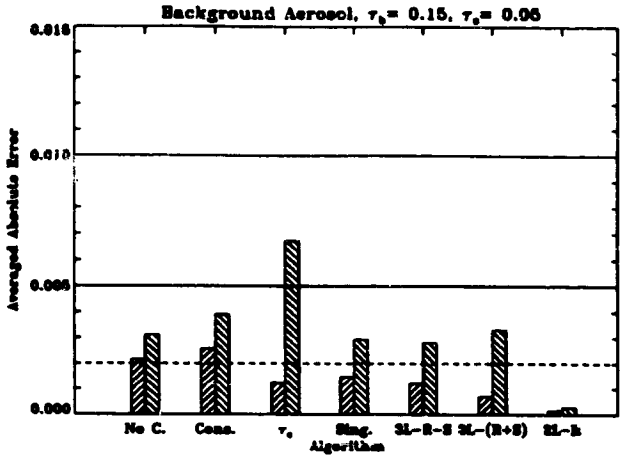

Figure 5a.

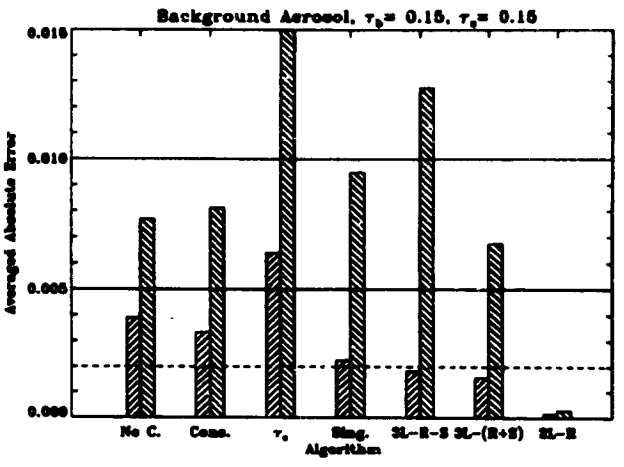

Figure 5b.

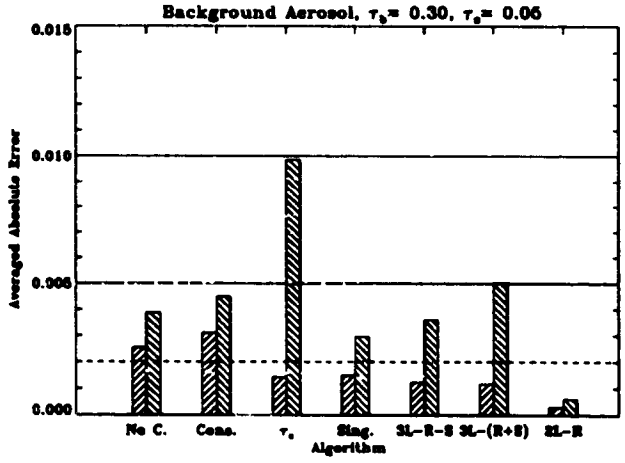

Figure 5c.

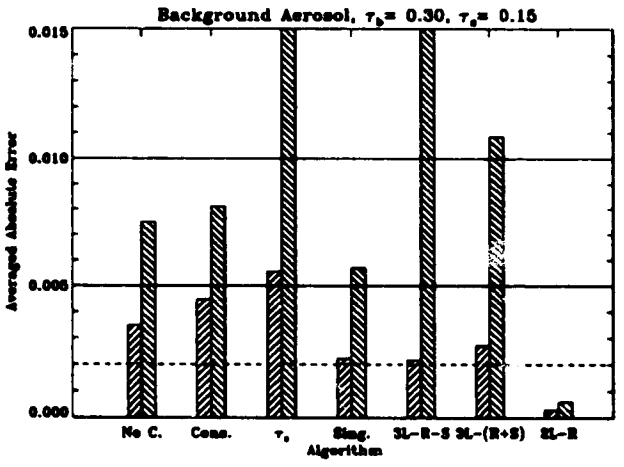

Figure 5d.

Figure 5. Histogram of the average $|\Delta t\rho_w(443)|$ (short bars) and the maximum $|\Delta t\rho_w(443)|$ (tall bars) for the Background stratospheric aerosol for various combinations of τ_b and τ_s: (a) $\tau_b(865) = 0.15$, $\tau_s(865) = 0.05$; (b) $\tau_b(865) = 0.15$, $\tau_s(865) = 0.15$; (c) $\tau_b(865) = 0.30$, $\tau_s(865) = 0.05$; and (d) $\tau_b(865) = 0.30$, $\tau_s(865) = 0.15$.

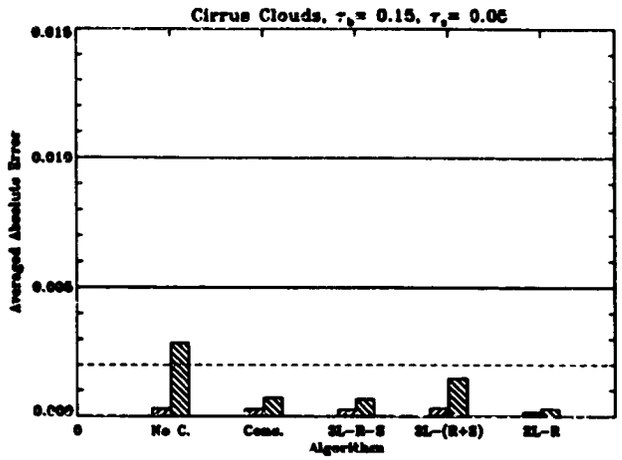

Figure 6a.

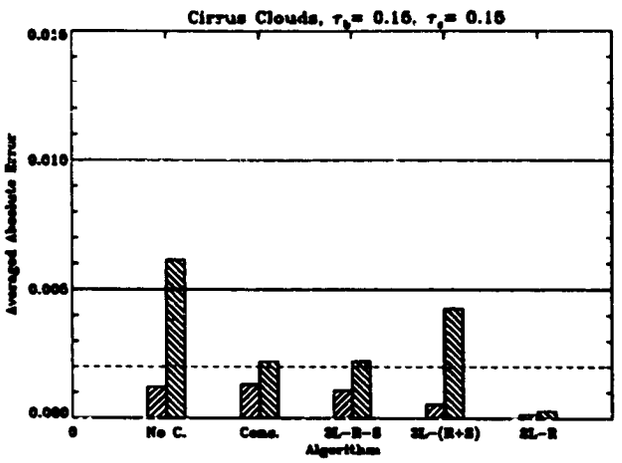

Figure 6b.

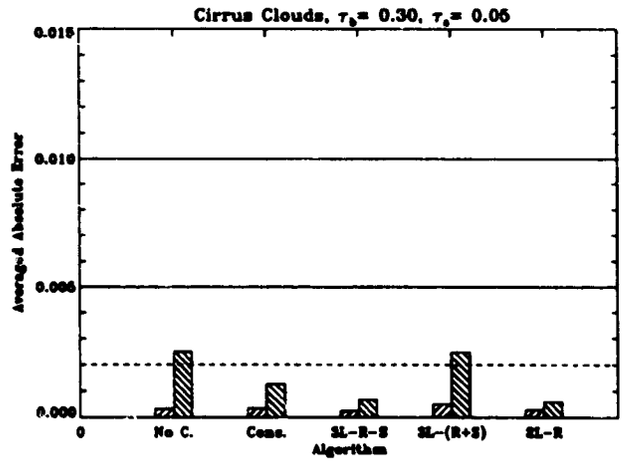

Figure 6c.

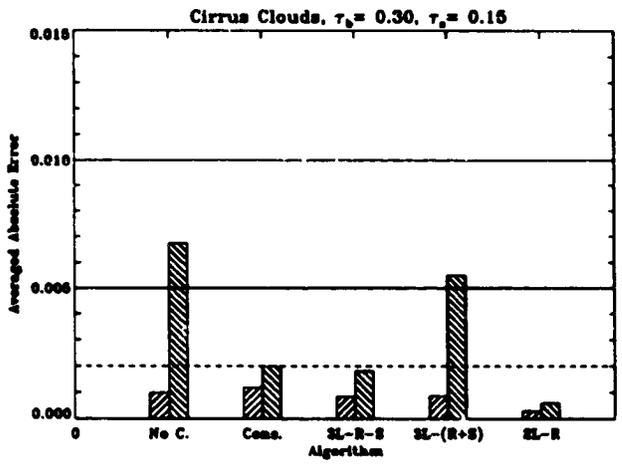

Figure 6d.

Figure 6. Histogram of the average $|\Delta t \rho_w(443)|$ (short bars) and the maximum $|\Delta t \rho_w(443)|$ (tall bars) for the cirrus clouds for various combinations of τ_b and τ_s: (a) $\tau_b(865) = 0.15$, $\tau_s(865) = 0.05$; (b) $\tau_b(865) = 0.15$, $\tau_s(865) = 0.15$; (c) $\tau_b(865) = 0.30$, $\tau_s(865) = 0.05$; and (d) $\tau_b(865) = 0.30$, $\tau_s(865) = 0.15$.

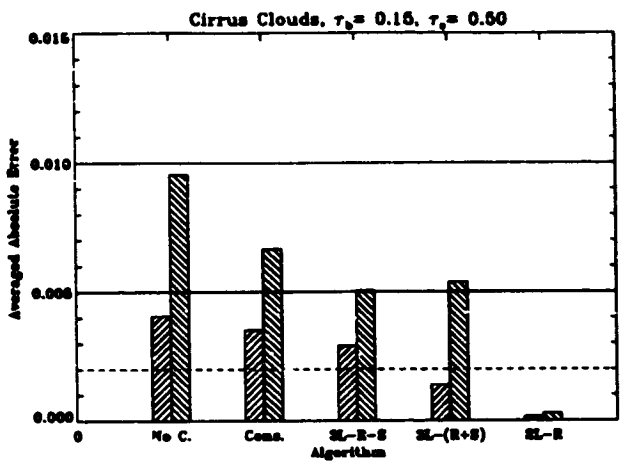

Figure 7a.

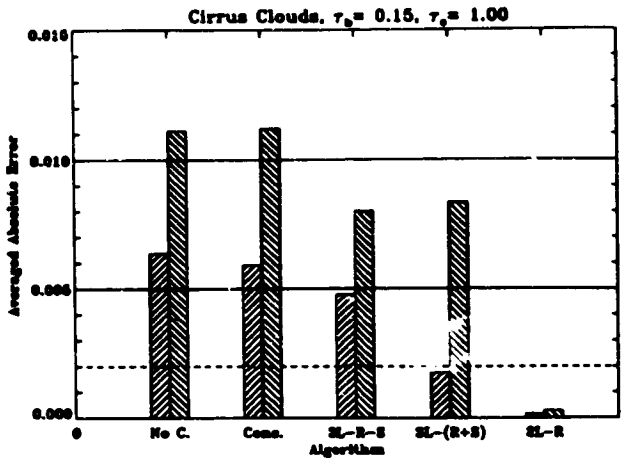

Figure 7b.

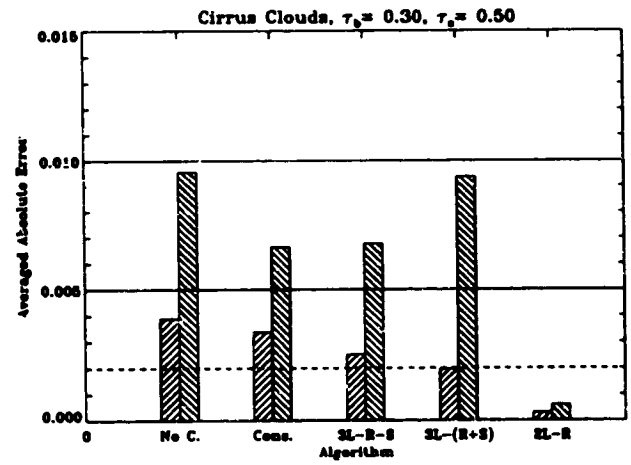

Figure 7c.

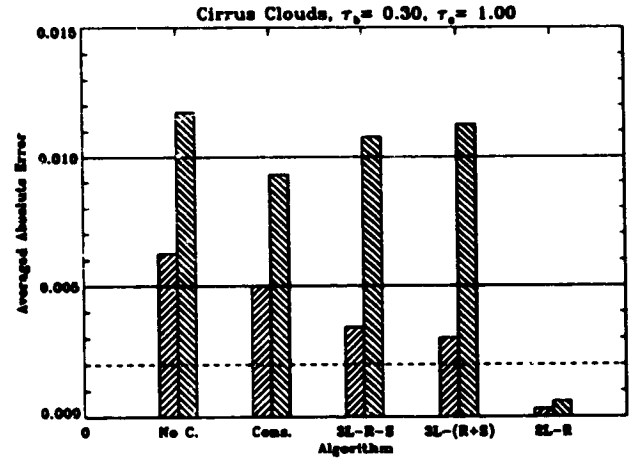

Figure 7d.

Figure 7. Histogram of the average $|\Delta t\rho_w(443)|$ (short bars) and the maximum $|\Delta t\rho_w(443)|$ (tall bars) for the cirrus clouds for various combinations of τ_b and τ_s: (a) $\tau_b(865) = 0.15$, $\tau_s(865) = 0.50$; (b) $\tau_b(865) = 0.15$, $\tau_s(865) = 1.00$; (c) $\tau_b(865) = 0.30$, $\tau_s(865) = 0.50$; and (d) $\tau_b(865) = 0.30$, $\tau_s(865) = 1.00$.